Stem Cell Reports
Resource
ISSCR
OPEN ACCESS

Reconstruction of dynamic regulatory networks reveals signaling-induced topology changes associated with germ layer specification

Emily Y. Su,[1,2,4] Abby Spangler,[1,4] Qin Bian,[1,2] Jessica Y. Kasamoto,[2] and Patrick Cahan[1,2,3,*]
[1]Institute for Cell Engineering, Johns Hopkins School of Medicine, Baltimore, MD 21205, USA
[2]Department of Biomedical Engineering, Johns Hopkins School of Medicine, Baltimore, MD 21205, USA
[3]Department of Molecular Biology and Genetics, Johns Hopkins School of Medicine, Baltimore, MD 21205, USA
[4]These authors contributed equally
*Correspondence: patrick.cahan@jhmi.edu
https://doi.org/10.1016/j.stemcr.2021.12.018

SUMMARY

Elucidating regulatory relationships between transcription factors (TFs) and target genes is fundamental to understanding how cells control their identity and behavior. Unfortunately, existing computational gene regulatory network (GRN) reconstruction methods are imprecise, computationally burdensome, and fail to reveal dynamic regulatory topologies. Here, we present Epoch, a reconstruction tool that uses single-cell transcriptomics to accurately infer dynamic networks. We apply Epoch to identify the dynamic networks underpinning directed differentiation of mouse embryonic stem cells (ESCs) guided by multiple signaling pathways, and we demonstrate that modulating these pathways drives topological changes that bias cell fate potential. We also find that *Peg3* rewires the pluripotency network to favor mesoderm specification. By integrating signaling pathways with GRNs, we trace how Wnt activation and PI3K suppression govern mesoderm and endoderm specification, respectively. Finally, we identify regulatory circuits of patterning and axis formation that distinguish *in vitro* and *in vivo* mesoderm specification.

INTRODUCTION

Gene regulatory networks (GRNs) model the regulatory relationship between a set of regulators, or transcription factors (TFs), and their target genes. The topology of these networks, defined by edges that map regulatory interactions between TFs and targets, offers a molecular-level view of a controlled system in which genes work together as part of a framework to accomplish specific cell functions (Karlebach and Shamir, 2008; Le Novère, 2015). Uncovering the topology of these GRNs is fundamental in answering a number of questions, including understanding how cellular identity is maintained and established (Davidson and Erwin, 2006), elucidating mechanisms of disease caused by dysfunctional gene regulation (Morgan et al., 2020; Qin et al., 2019), and finding novel drug targets among others (Carro et al., 2010). In the context of cell fate engineering, the mapping of GRNs would enable the identification of TFs required to activate the expression of target genes so as to control cell fate transitions or cell behavior (Cahan et al., 2021; Rackham et al., 2016). Unfortunately, how best to map these relationships remains both an experimental and a computational challenge.

Experimental approaches, including chromatin immunoprecipitation sequencing (ChIP-seq), have identified regulatory targets and TF binding site motifs in certain cell lines and cell types. Similarly, chromatin accessibility assays that detect TF-binding site (TFBS) footprints, such as assay for transposase-accessible chromatin with high-throughput sequencing (ATAC-seq) (Buenrostro et al., 2013), enable the inference of regulatory networks. However, these approaches are limited in scope (e.g., ATAC-defined networks are limited to TFs with known motifs) and scalability (e.g., it is infeasible to perform ChIP-seq for all TFs in all cell types). Therefore, computational methods to infer GRNs are needed. Methods that leverage advances in data collection and machine learning to enable the statistical inference of GRNs via gene expression data include those based on information theory (Faith et al., 2007; Margolin et al., 2006; Meyer et al., 2007), ensemble learning (Huynh-Thu et al., 2010), Bayesian theory (Hartemink, 2005; Yu et al., 2004), and ordinary differential equations (ODEs) (di Bernardo et al., 2005). Unfortunately, the tools developed to date suffer from several drawbacks, including low precision and sensitivity. The leading contributors to poor performance include difficulty in distinguishing direct from indirect interactions (Marbach et al., 2010), the confounding effects of Simpson's paradox (Trapnell, 2015), and the fact that bulk derived data does not offer perturbation sufficient to detect regulatory relationships (Stark et al., 2003). Attempts to ameliorate these by aggregation across methods have achieved modest success (Marbach et al., 2012).

With the advent of single-cell RNA-seq (scRNA-seq) (Klein et al., 2015; Macosko et al., 2015; Zheng et al., 2017), computational techniques have emerged that try to take advantage of the resolution offered by single-cell transcriptomics to infer GRN structures (Aibar et al., 2017; Matsumoto et al., 2017; Qiu et al., 2020). To date, these methods suffer from limitations similar to those of

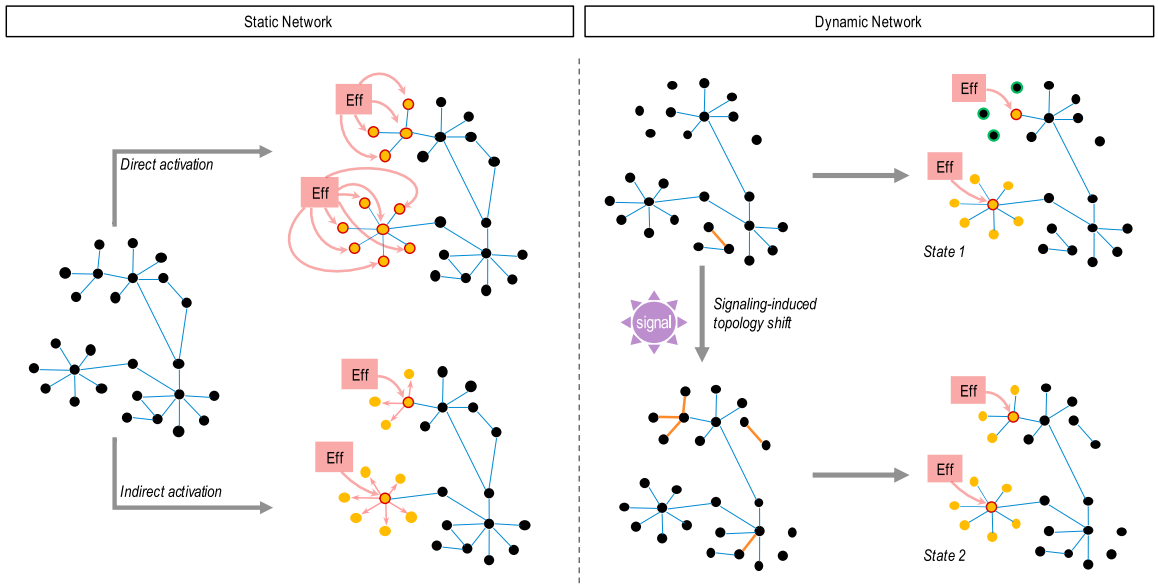

Figure 1. Effector activity on static and dynamic networks

Given a static GRN, manipulating signaling activity may result in an effector guiding cell state via two possibilities: directly, the effector may regulate a set of fate-specific genes, or indirectly, the effector may regulate a set of TFs that further regulate the same fate-specific genes. Both cases result in the activation of the same program. Alternatively, given a dynamic network, the state space of possible cell fates increases since the result of effector activity is dependent on a changing network topology. As a result, multiple sets of genetic programs may be regulated through the same signaling mechanism. Furthermore, these shifts in GRN topology maybe be induced by the signaling activity itself.

their bulk counterparts, including low precision and sensitivity (Chen and Mar, 2018) and high computational burden, which limits users' ability to hone analysis through iterative application (Bonnaffoux et al., 2019). In addition to higher resolution and access to more perturbations, single-cell data allow for computational modeling of dynamic processes, such as differentiation, by ordering cells along a trajectory following linear or more complex graph structures (Haghverdi et al., 2016; Qiu et al., 2011; Street et al., 2018; Trapnell et al., 2014). While many new scRNA-seq GRN methods use pseudotemporal analysis to aid in reconstruction, they are limited in their ability to explain how network topology evolves over time. We define a dynamic topology as one that changes the edge-level regulatory relationships between TFs and targets over time, which thereby increases the number of reachable cell states (Figure 1). This implies that for a given TF-target relationship, the modulation of the TF in a particular context or time point would lead to changes in target expression, but modulation of the same TF in another context or time point would not lead to changes in target expression. The dynamic and noncommutative nature of regulatory networks permits independent control of genetic programs that would otherwise be simultaneously activated with non-sequential, or combinatorial, logic (Letsou and Cai, 2016). Such shifts in network topology can arise for several reasons, including the presence or absence of co-factors, epigenomic modifications, or changes in chromatin accessibility. Thus, for GRNs to more accurately model the emergence of distinct cell fates, they must encapsulate this dynamic behavior of changing GRN topology. Moreover, because GRN topology dictates how a cell responds to perturbation, uncovering the dynamic GRN aids in understanding how the landscape of reachable cell states changes over time, which has implications in the quest to engineer cell fate.

For those reasons, we developed a computational GRN reconstruction tool called Epoch, which uses single-cell transcriptomics to efficiently reconstruct dynamic networks. There are several features that distinguish Epoch from other methods: first, reconstruction is limited to dynamically expressed genes. Second, Epoch uses an optional "cross-weighting" strategy to reduce false positive interactions. Third, Epoch divides pseudotime into epochs, or discrete time periods, extracts a dynamic network, and predicts the most influential regulators in driving topology changes. Finally, Epoch includes a number of functionalities to aid in network analysis and comparison, including the integration of GRNs with major signaling pathways and subsequent tracing through the

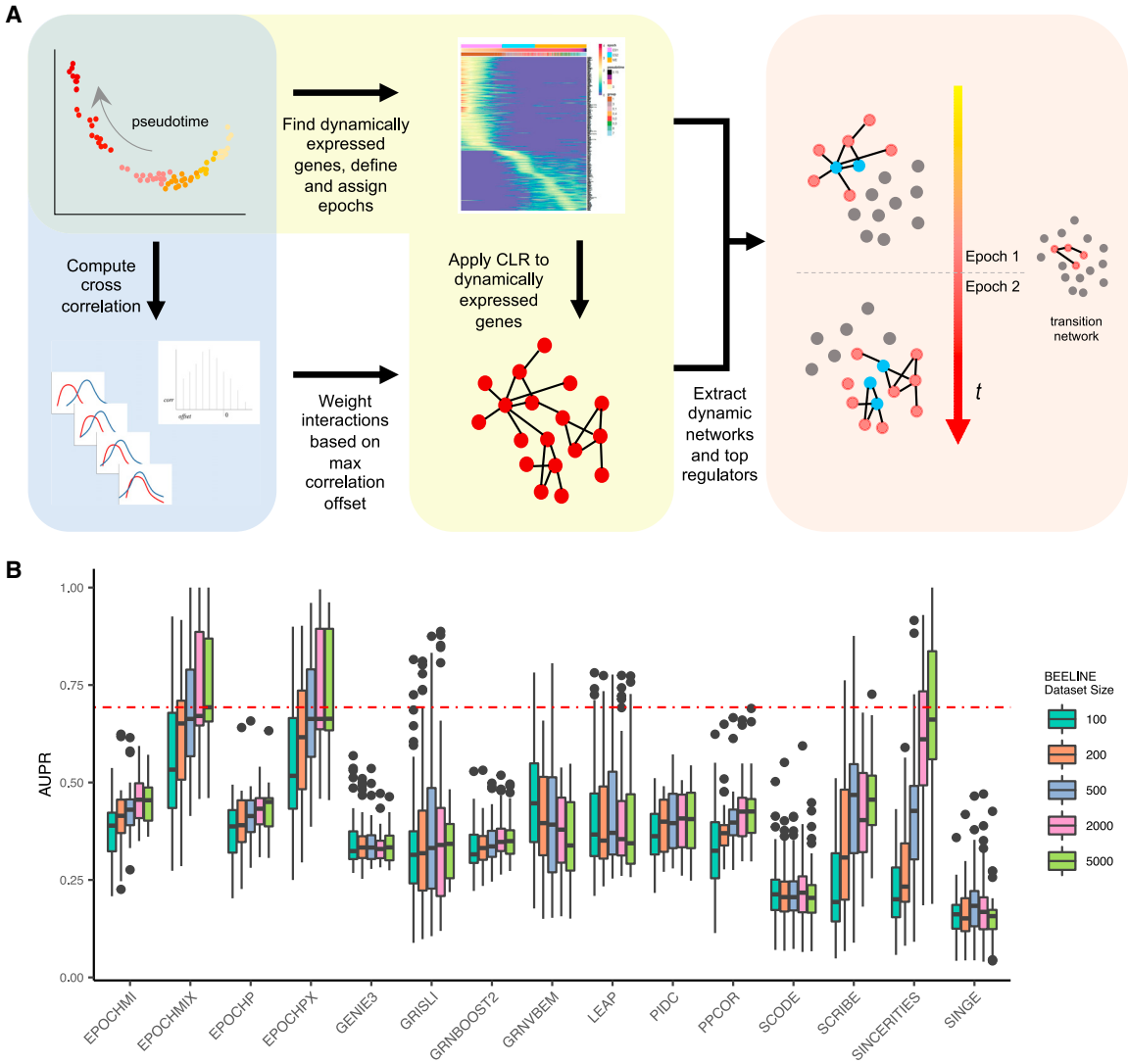

Figure 2. Epoch workflow and benchmarking

(A) Epoch relies on a 3-step process to reconstruct dynamic network structures: (1) extraction of dynamic genes and CLR, (2) application of cross-weighting, and (3) extraction of the dynamic network.

(B) BEELINE benchmarking on synthetic data. Epoch using mutual information (MI) and Pearson, denoted by "MI" and "P," respectively. "X" indicates the use of cross-weighting. The red line indicates the median AUPR of the best-performing method, Epoch using MI + cross-weighting on size 5,000 cell datasets. Kruskal-Wallis $p < 2.2 \times 10^{-16}$. See also Figures S2 and S3.

GRN of the shortest paths from signaling effectors to selected target genes. We compared the performance of Epoch to commonly used computational GRN reconstruction tools using synthetically generated data, *in vivo* mouse muscle development data, and *in vitro* directed differentiation data. To demonstrate the utility of Epoch, we applied it to mouse embryonic stem cells (ESCs) undergoing directed differentiation to measure the extent to which signaling pathways influence cell fate by altering GRN topology rather than by direct regulation of pathway effectors (Figure 1).

RESULTS

Epoch relies on single-cell analysis techniques to infer dynamic network structures

Epoch takes as minimum input processed single-cell transcriptomic data and pseudotime or equivalent annotation from any trajectory inference method (Figure 2A). Its first step is to limit reconstruction to dynamically expressed genes to focus on genes playing an active role in cell state changes. To accomplish this, Epoch models gene expression across pseudotime using a generalized additive model.

Upon filtering the data for dynamically expressed genes, Epoch reconstructs an initial static network via a CLR-like (Context Likelihood of Relatedness) method, using either Pearson correlation or mutual information (MI) to infer interactions (Faith et al., 2007).

In an optional step, which we have called "cross-weighting," Epoch next refines the network via a cross-correlation-based weighting scheme. This helps to reduce false positives that may result from indirect interactions or that represent non-logical interactions, ultimately improving precision (Figure S1A). In this step, the expression profiles over pseudotime for each TF-target pair are aligned and progressively shifted to determine an average offset value at which maximum correlation is achieved between the two profiles. A graded-decline weighting factor is computed based on this offset, and it is used to negatively weight interactions that are less likely to be true positives.

Once a static network has been inferred, Epoch extracts a dynamic network. This begins with Epoch breaking down pseudotime into epochs, based on pseudotime, cell ordering, k-means or hierarchical clustering, sliding window similarity, or user-defined assignment. With the exception of user-defined assignment, all methods of defining epochs are, to some extent, automated, with epoch definitions learned directly from the data. Genes are assigned to epochs based on their activity along pseudotime. Epoch then fractures the static network into a dynamic one, composed of "epoch networks," representing active interactions within a particular epoch, and "transition networks," describing how an epoch network transitions into a subsequent epoch network.

As Epoch was initially built with the improvement of cell fate engineering protocols in mind, we included in the framework network analysis and comparison capabilities. For example, Epoch will identify influential TFs within a given static or dynamic network by extracting top regulators that appear to have the most influence on network state. Specifically, Epoch ranks TFs by PageRank (Brin and Page, 1998) in the context of their epoch networks, and will also look for TFs that simultaneously score high in betweenness and degree centralities as compared to all of the other TFs. In addition, Epoch can integrate major signal transduction pathways with reconstructed networks. This can be used to determine the shortest paths through the networks from pathway effectors to groups of specified target genes, allowing users to identify topologies capable of activating or repressing specific groups of genes.

Finally, Epoch is modularly designed such that it can be broken into individual steps and flexibly merged and used with any trajectory inference, network reconstruction, and network refinement tools.

To assess the performance of Epoch in reconstructing static networks, we benchmarked it against multiple variations of CLR (Faith et al., 2007) and GENIE3 (Huynh-Thu et al., 2010) (including the original methods themselves and variations in which the methods were embedded within the Epoch framework) on *in vivo*, *in vitro*, and *in silico* datasets (Figure S2; Note S1). Our results indicated that key steps in the Epoch framework improved overall static network reconstruction, as limiting reconstruction to dynamically expressed genes and applying the cross-weighting scheme both led to increased fold improvement in area under the precision-recall curve (AUPR) over random. We further compared Epoch to recently developed GRN reconstruction methods designed for single-cell data. We used the benchmarking platform BEELINE (Pratapa et al., 2020) to assess the performance of Epoch against 11 other single-cell methods across synthetic and curated datasets (Figures 2B and S3). Our results demonstrated that Epoch with cross-weighting outperformed all other methods based on AUPR and execution time.

scRNA-seq of early *in vitro* mouse ESC-directed differentiation

With the goal of exploring the dynamic GRN topology underlying lineage specification in gastrulation, we collected scRNA-seq data from days (d) 0 through 4 of *in vitro* mESC-directed differentiation guided by four separate treatments encouraging primitive streak formation (Figure 3A). Briefly, cells were allowed to differentiate in serum-free differentiation media before being treated with 1 of 4 treatments on d2: Wnt3a and activin A alone (WA), or with one of Bmp4 (WAB), GSK inhibitor (WAG), or Noggin (WAN). Multiple rounds of differentiation were staggered such that we could harvest samples representative of d0–d4 at one time for sequencing using the MULTI-seq protocol (McGinnis et al., 2019). After barcode classification, samples were preprocessed using the SCANPY pipeline (Wolf et al., 2018), and RNA velocity analysis was performed (Bergen et al., 2020; La Manno et al., 2018) (Figures 3B and 3C).

We detected three distinct lineages, neuroectoderm (based on *Sox1* expression), mesoderm (*Mesp1*), and endoderm (*Foxa2*), a result confirmed by comparison to gastrulation data with SingleCellNet (SCN) (Tan and Cahan, 2019) (Figures 3D and S4; Table S1; Note S2). RNA velocity additionally supported our cluster annotations. We found that the majority of the differentiating cells transitioned toward the neuroectoderm (clusters '0,2', '0,3', 4, 2, 5, 9), with smaller populations transitioning toward mesoderm (cluster 8) and endoderm (clusters '7,1' and '7,0').

We observed differences between induction treatments in terms of the distribution of cells among the different populations (Figures 3E and 3F). Notably, cells treated with WAG exhibited a stunted trajectory toward neuroectoderm but a fuller trajectory toward mesoderm. This was

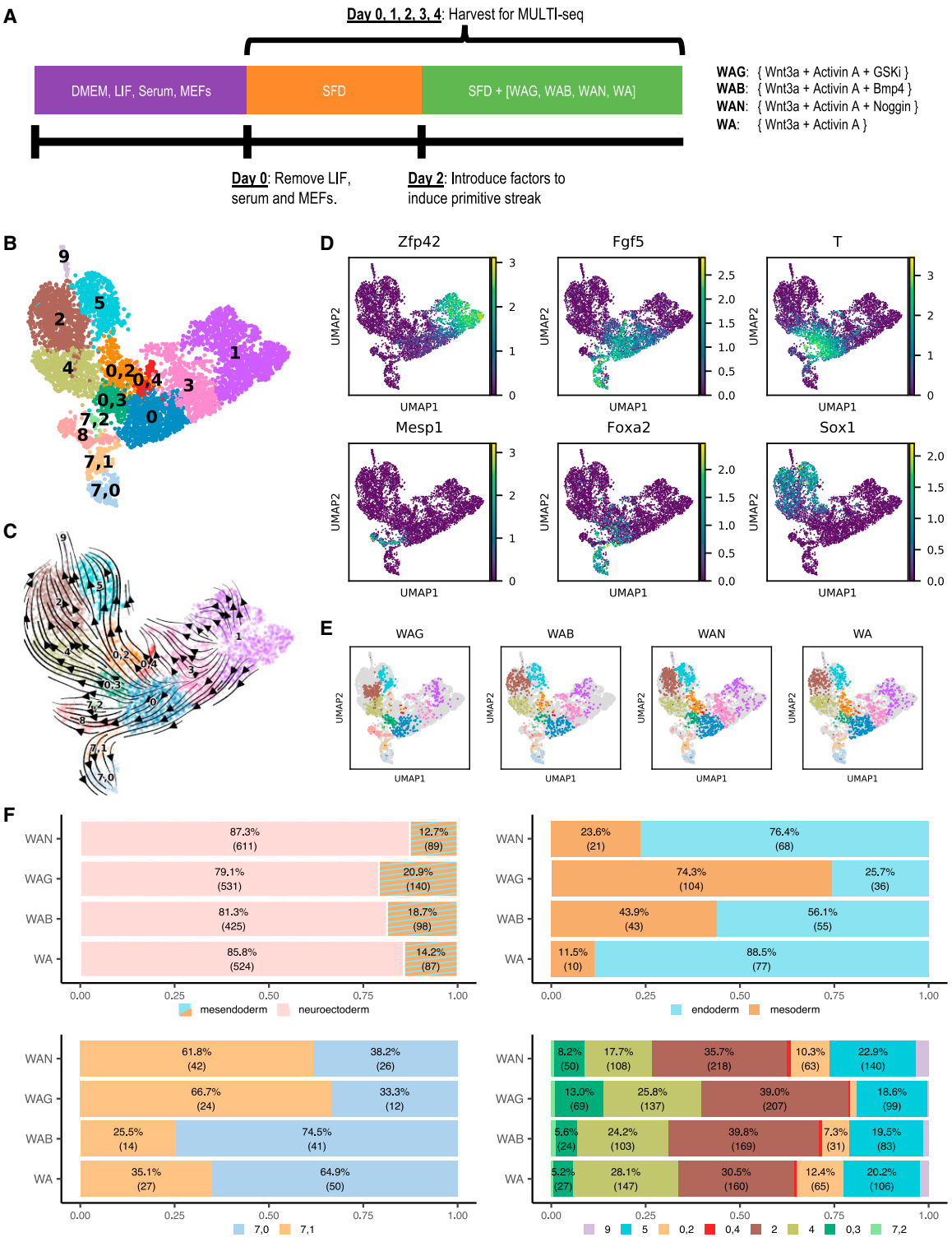

Figure 3. mESC *in vitro*-directed differentiation

(A) Directed differentiation protocol. Cells were harvested from d0 through d4 samples for MULTI-seq.

(B and C) Clustering (B) and (C) RNA velocity for MULTI-seq data.

(D) Select marker gene expression. See also Figure S4C.

(E) Cell populations by treatment.

(F) Quantification of cell fate distribution based on treatment comparing mesendoderm and neuroectoderm, endoderm and mesoderm, cluster '7,0' and '7,1' along endoderm fate, and cluster distribution along neuroectoderm fate.

in contrast to cells treated with the remaining three treatments (WAB, WAN, and WA), in which very few cells differentiated toward mesodermal fate, but instead exhibited strong neuroectodermal or endodermal commitment. Furthermore, while WAB and WA cells tended to transition into cluster '7,0' (furthest along endodermal development), WAN and WAG cells were more likely to stay in cluster '7,1'.

We applied Epoch to reconstruct the networks underlying the data, using latent time (Bergen et al., 2020) to order cells. Latent time was divided into three epochs, a dynamic network was extracted for each lineage, and top regulators were extracted via PageRank and Betweenness-Degree (Figure S5; Table S2; Note S3).

Peg3 is a central regulator in mesodermal WAG networks

We next asked why WAG-treated cells had the greatest propensity for mesoderm fate. We hypothesized that treatment-specific GRNs underpinned differences in fate potential among treatments. To explore this hypothesis, we reconstructed and compared dynamic networks for each treatment along the mesodermal path (which we refer to as the treatment-specific networks: WAG, WAB, WAN, and WA networks), and we compared these against the full reconstructed mesoderm network, which is reconstructed from all cells regardless of treatment, and which we refer to as the mesoderm network.

We sought to identify regulators that drive differences in mesoderm reachability between the treatments. We performed community detection on epoch 2, epoch 3, and their transition of the mesoderm network and identified distinct TF communities, or modules (Figures 4A and S6A). We assessed the activity of each module by looking at the average expression of member genes across latent time for each treatment (members predicted to be repressed were not included in the average so as not to improperly depress this measure of activity) (Figures 4B and S6B). At least three modules exhibited strong activation in the WAG treatment, but were inactive or weakly activated in the remaining three treatments. The TFs in these modules were *Peg3*, *Lhx1*, *Hoxb2*, *Foxc1*, *Tshz1*, *Meis2*, *Mesp1*, *Tbx6*, *Foxc2*, *Prrx2*, *Meox1*, and *Notch1*. Upon extracting the differential network, defined as the network containing the interactions that are more specific to a treatment network by edge weight (see supplemental experimental procedures), between WAG and WA, we identified the top differential regulators of these TFs themselves (Figures 4C and S6C). Interestingly, *Peg3* was an upstream regulator of the majority of these TFs in the WAG treatment, but had a negligible role in the WA treatment.

The central influence of *Peg3* in the WAG network implied a pathway linking glycogen synthase kinase 3 (GSK3) inhibition, *Peg3* expression, and mesodermal gene expression. GSK3 contributes to DNA methylation at imprinted loci, including *Peg3*, in mESCs via *Dnmt3a* (Meredith et al., 2015), potentially mediated by *N-Myc* (Popkie et al., 2010). Consistent with a model whereby GSK3 maintains repressive methylation of *Peg3* via *Dnmt3a* activity, we found that *Dnmt3a* and *Peg3* expression were largely mutually exclusive, and there was low-to-no *Dnmt3a* expression in the WAG-treated cells (Figure S6D). This phenomenon occurs *in vivo*, too, as we found a relatively high expression of *Dnmt3a* in epiblast cells, which was tapered in primitive streak and mesodermal cells (Figure 4D) from a single-cell mouse gastrulation dataset (Grosswendt et al., 2020). In contrast, *Peg3* expression was low in epiblast and increased in the primitive streak, mirroring our *in vitro* data, and suggesting that *Peg3* may have a role in orchestrating the exit of pluripotency and specification of mesodermal fate *in vivo*.

Tracing signaling cascades to germ layer transcriptional programs

We next sought to trace pathways from signaling effectors to the activation of mesodermal fate. To determine which signal transduction pathways were active and when along the mesodermal trajectory, we computed the average expression of targets of 18 signaling effector TFs (available as part of the Epoch framework) across latent time broken down by treatment. As expected, targets of the Wnt effector Lef1 were activated early in WAG, whereas targets of the transforming growth factor-β (TGF-β)/bone morphogenetic protein (BMP) effector Smad4 were activated to the highest extent and longest duration in WAB (Figure 5A). Notch targets were activated in WAB, WAN, and WA, but not in WAG, along the mesodermal lineage (and weakly activated along the neuroectodermal lineage), consistent with the role of Notch in specifying neuroectodermal fate in the neuroectoderm-mesendoderm fate decision (Androutsellis-Theotokis et al., 2006; Aubert et al., 2002).

Because Wnt signaling is essential for mesodermal fate, we looked for paths connecting Wnt effectors to the TFs in the WAG-specific modules defined previously. We computed the shortest paths from targets of Wnt effectors to the module TFs in each treatment-specific dynamic network (using edge lengths inversely proportional to the cross-weighted score) (Figure 5B), finding that no paths from Wnt to many of the module TFs existed in WAB, WAN, and WA.

Our signaling effector target analysis also revealed increased *Foxo1* activity in WAB-, WAN-, and WA-treated cells as compared to WAG-treated cells, indicating the suppression of phosphatidylinositol 3-kinase (PI3K) signaling along the WAB, WAN, and WA trajectories (Figure 5A). The establishment of definitive endoderm (DE) requires the

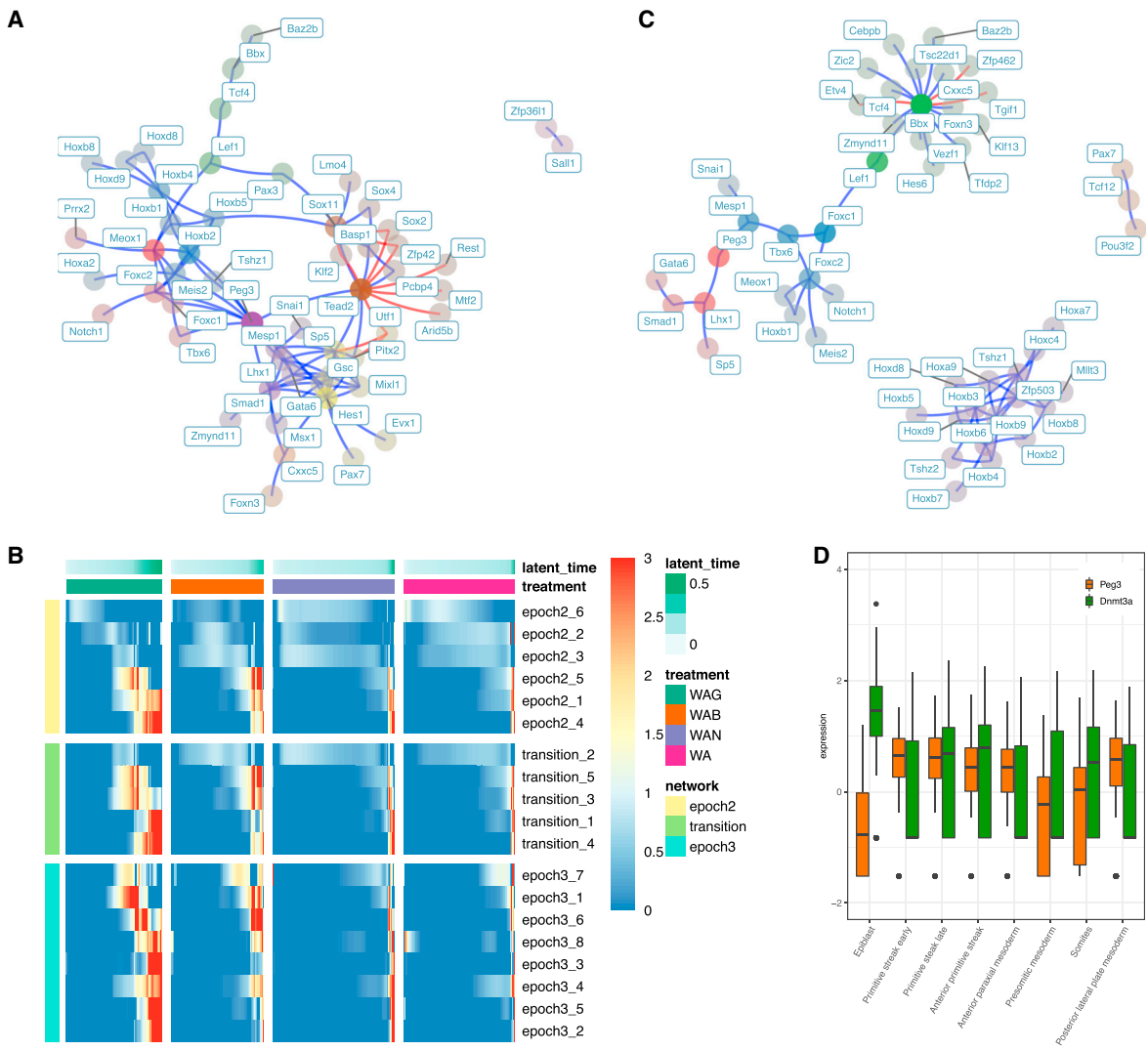

Figure 4. Mesodermal network analysis

(A) The epoch 3 subnetwork of the mesodermal dynamic GRN. TFs are colored by community and faded by betweenness. Blue and red edges represent activating and repressive edges, respectively.

(B) Average community expression over time by treatment along the mesodermal path. Communities shown (each row) are from the epoch 2 subnetwork (yellow), transition (green), and epoch 3 subnetwork (aqua).

(C) The epoch 3 differential network between WAG and WA. Interactions in this network represent edges present in the WAG mesodermal network that are not present in the WA mesodermal network. TFs are colored by community and faded by betweenness. Blue and red edges represent activating and repressive edges, respectively.

(D) *Peg3* and *Dnmt3a* expression in a sampled portion of relevant cell types in gastrulation data adapted from Grosswendt et al. (2020). *Peg3* ANOVA $p < 2 \times 10^{-16}$, *Dnmt3a* ANOVA $p < 2 \times 10^{-16}$.

suppression of PI3K signaling (McLean et al., 2007; Yu et al., 2015), and in induced pluripotent stem cell (iPSC)-DE differentiation *Foxo1* binds to DE-formation-related genes and its inhibition impedes DE establishment (Nord et al., 2020). We therefore hypothesized that a second fate choice between mesodermal and endodermal fates further exacerbated the uneven mesodermal fate preference between the treatments. Our analysis indicates that in the mesodermal-endodermal fate choice, the majority of WAG-treated cells differentiate toward the mesoderm in contrast to WAN and WA in which cells preferentially differentiate toward DE. WAB-treated cells exhibited a mixed potential split roughly equally along the two paths.

We sought to elucidate a possible explanation for the role of *Foxo1* in this fate choice by searching for the shortest paths toward a set of endodermal genes. Specifically,

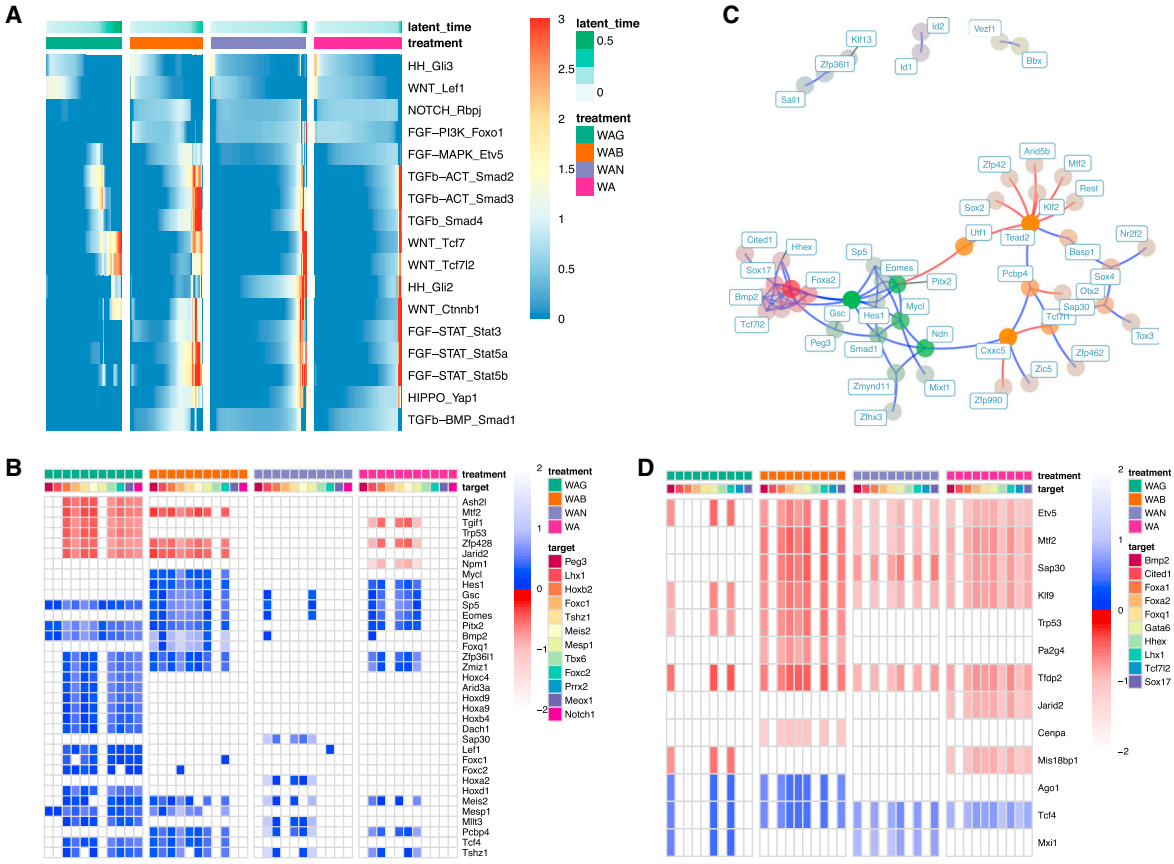

Figure 5. Integrating signaling effectors and tracing paths to target genes

(A) Average expression of targets of signaling effectors by treatment over time. Pathway and effector are labeled on each row.

(B) Shortest path analysis showing length of shortest paths from Wnt effector targets (each row) to mesodermal target genes (each column) within treatment-specific networks. Path lengths are normalized against average path length within a network. Blue and red indicate paths that activate and repress the target gene, respectively. If such a path does not exist, then it has length of infinity and is therefore white.

(C) The epoch 3 subnetwork of the endodermal dynamic network. TFs are colored by community and faded by betweenness. Blue and red edges represent activating and repressive edges, respectively.

(D) Shortest path analysis showing length of shortest paths from PI3K suppression (targets of *Foxo1* activation) (each row) to endodermal genes (each column) within treatment-specific networks. As before, path lengths are normalized against average path length within a network. Blue and red indicate activation and repression of the target gene, respectively. If a path does not exist, it has length of infinity and is therefore white.

similar to the previous mesodermal analysis, we applied community detection to the full endodermal network and identified the cluster containing *Sox17* and *Foxa2*, known master regulators of endodermal fate (Figure 5C). This cluster included the TFs *Sox17*, *Foxa2*, *Bmp2*, *Cited1*, *Foxa1*, *Gata6*, *Hhex*, *Lhx1*, and *Tcf7l2*. For each treatment-specific network, we computed the shortest paths from *Foxo1* targets to these genes (Figure 5D). We found that many of these regulators, including both *Sox17* and *Foxa2*, were not reachable from *Foxo1* in the WAG network, consistent with the observation that WAG-treated cells preferentially differentiated toward mesodermal fate over endodermal fate. Interestingly, *Foxa2* was not reachable in the WAN network, although *Sox17* was. We believe this may explain the differences in the distribution of cells between the endodermal clusters '7,1' and '7,0'. Of the cells that specify endodermal fate, WA- and WAB-treated cells more fully transitioned into cluster '7,0'. In contrast, WAN-treated cells remained mostly in cluster '7,1' and were less likely to differentiate further into '7,0' . Previous studies in directed differentiation of human ESCs toward DE have implicated a regulatory role of *Sox17* in establishing DE to be upstream of *Foxa2*, the loss of which impairs foregut and subsequent hepatic endoderm differentiation

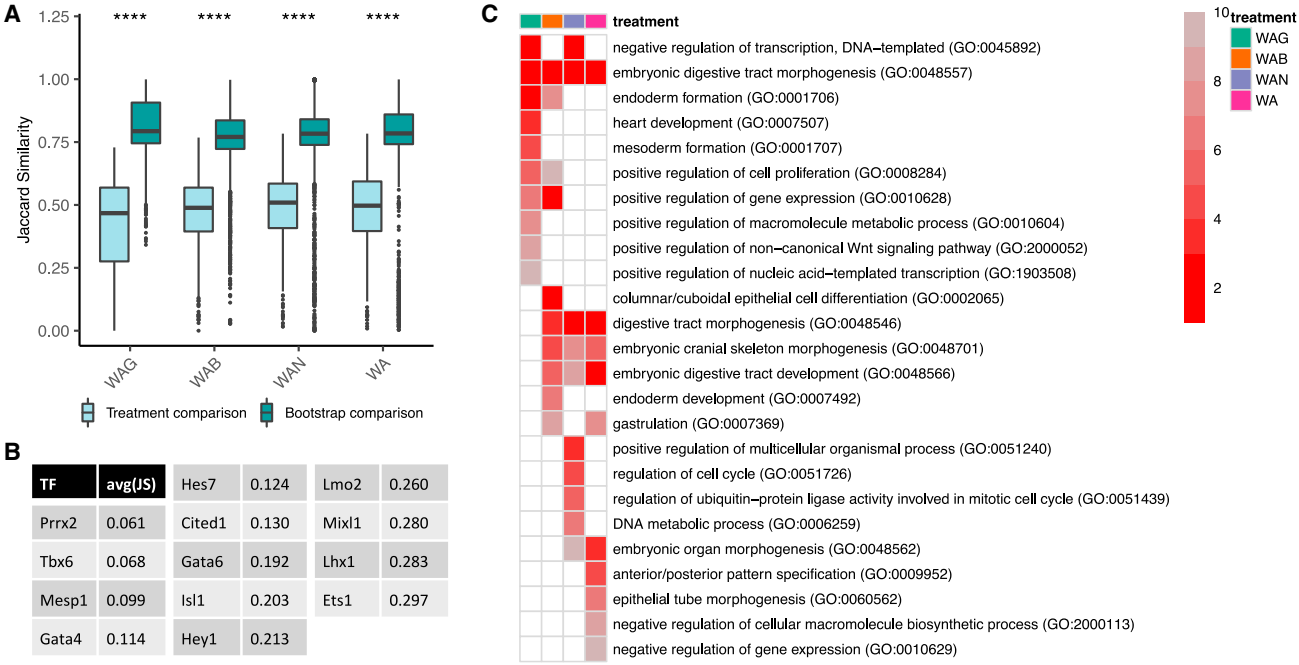

TF	avg(JS)				
Prrx2	0.061	Cited1	0.130	Mixl1	0.280
Tbx6	0.068	Gata6	0.192	Lhx1	0.283
Mesp1	0.099	Isl1	0.203	Ets1	0.297
Gata4	0.114	Hey1	0.213		

Figure 6. Similarity of targets of TFs in different treatments

(A) Jaccard similarity of targets of 72 TFs. The targets of each TF in a treatment are compared to those in the other 3 treatments (light blue). As a baseline (turquoise), targets of each TF in bootstrapped reconstructed networks within a treatment are pairwise compared. All pairs $p < 2 \times 10^{-16}$.

(B) The 13 TFs selected for GSEA and their average pairwise Jaccard similarity among the treatment-specific networks.

(C) Summarized results of performing GSEA on targets of TFs in (B). Heatmap shows rankings (top 10 shown) based on the frequency a term is considered enriched among the 13 TFs (1 = most frequently enriched term).

(Genga et al., 2019). This is consistent with our cell-type annotations of cluster '7,1' (definitive endoderm) and '7,0' (gut endoderm), and offers a possible mechanism of the discrepancy in cell fate preferences between treatments. These results demonstrate that WAB, WAN, and WA networks do not allow for the activation of mesoderm programs from their cognate effectors, but instead assume topologies that are preferential for endodermal fate, implying profound structural changes in the networks that underlie the treatment-specific differences we see in cell fate. Furthermore, this analysis provides a basis for identifying which signaling pathways must be targeted for directing certain fate transitions—for example, through an exhaustive search of effector targets.

TF-target gene differences among treatments illuminate rewiring of network topology by signaling pathways

Given the apparent restructuring of GRN topology by signaling activity, we aimed to understand the extent to which network-wide topology changes were responsible for differences in cell fate potential between treatments. To answer this, we performed two analyses focusing on the differences in targets of TFs across the four treatment networks.

First, we asked whether TFs actively expressed in all four treatments regulated the same set of target genes. To this end, we focused on the treatment-specific networks along the mesodermal path, and narrowed our analysis to the 72 TFs that were active in all 4 treatments during d3 or d4. We quantified the overlap between the targets of each TF in a pairwise comparison of the treatments using the Jaccard similarity (Figure 6A). As a baseline, we implemented a bootstrapping method in which we reconstructed 10 networks for each treatment (using 400 sampled cells each); for each TF, we calculated the average Jaccard similarity of its targets among pairwise comparisons of the reconstructed networks within a treatment. This gave us a baseline, or expected, Jaccard similarity for each TF in each treatment. Overall, we found that overwhelmingly, target differences between treatments were significantly greater than the baselines, indicating vast network topology differences among the treatment networks.

Second, we asked whether these differences in predicted targets had functional consequences in affecting fate potential. To this end, we focused on the 13 TFs among the

72 mentioned above that exhibited the largest differences in predicted targets between treatments (Figure 6B). For each treatment, we performed gene set enrichment analysis (GSEA) on the predicted targets of these TFs (Figure 6C). In line with our observations, we found enrichment for heart development and mesoderm formation in only the WAG treatment, despite the fact that the networks we analyzed were reconstructed along the mesodermal path. Our results are consistent with previous literature that hinted at environment-based differences in the fate potential of mESCs in that Esrrb/Nanog double knockdown impedes self-renewal in 2i alone but not in the presence of 2i and leukemia inhibitory factor (LIF) (Dunn et al., 2014). These results support our hypothesis that manipulating signaling activity results in a topological restructuring of the GRN, ultimately guiding cell fate potential.

Patterning and neuroectoderm programs drive differences between *in vivo* and *in vitro* gastrulation and mesoderm specification

Finally, we aimed to understand the extent to which our *in vitro* mESC-derived mesodermal cells established a GRN resembling that of their *in vivo* counterparts. To this end, we sampled 250 cells from previously published gastrulation stage embryos for each of 4 annotated populations that corresponded to our *in vitro* mesoderm lineage populations: Epiblast, Primitive streak early, Primitive streak late, and Mesoderm presomitic. We then used Epoch to reconstruct an *in vivo* dynamic network from these sampled data. After reconstruction, we extracted the top regulators in each epoch (Figure 7A). Of the 22 unique top regulators in epochs 2 and 3, at least 17 have known roles in guiding exit from pluripotency, mesoderm specification, or somitogenesis (Note S4), corroborating the usefulness of Epoch in identifying important TFs driving dynamic processes. Of note, *Peg3* ranked highly in epoch 2 of the *in vivo* network, bolstering our earlier prediction of Peg3 as an orchestrator of the pluripotent-to-mesodermal fate transition *in vitro* and *in vivo*.

Substantial differences between top regulators of the *in vivo* and *in vitro* networks suggested broader topology differences. Thus, we further applied the signaling pathway tracing analysis to the *in vivo* network. Analogous to the *in vitro* networks, we looked for paths connecting Wnt effectors to the same TFs in the *in vitro* WAG-specific modules (Figure 7B). As expected, all of the TFs were reachable. Furthermore, Wnt activation and these target TFs were highly connected, with paths existing from almost every effector target to every TF, implying the existence of robust and coordinated control over this mesoderm module.

Finally, we sought to directly compare the topological and functional differences between the *in vivo* and *in vitro* mesoderm networks. To directly compare topological differences, we applied a threshold to both networks, keeping the top 2% of non-zero-weighted edges in each. We then extracted the differential network corresponding to the *in vivo*-specific interactions and the differential network corresponding to the *in vitro*-specific interactions (data not shown). We performed community detection on both and measured the activity of each resulting module by assessing the average expression of member genes across time in the *in vivo* and *in vitro* data (Figures S7A and S7B).

Of the *in vivo*-specific modules, three had low or insignificant activation in the *in vitro* data, despite being strongly activated in the *in vivo* data. To understand the functional consequences of this, we applied GSEA to each of these modules (Figures 7C and S7C). Two modules showed enrichment for multiple pathways related to patterning and axis specification. Thus, a large but not unexpected difference between the *in vivo* and *in vitro* mesoderms is the lack of activation of patterning programs in the *in vitro* ESC-derived mesodermal cells.

Conversely, of the *in vitro*-specific modules, we isolated those that had low or insignificant activation in the *in vivo* data but were strongly activated in the *in vitro* data. Within the first epoch, three communities satisfied this criterion. We hypothesized that differences in this early epoch could drive fate differences between the two networks at a later time. GSEA on these modules revealed that one was enriched for the positive regulation of stem cell proliferation and the regulation of mRNA splicing, while another was enriched for terms related to fluid shear stress, DNA methylation, and male gonad development (Table S3). Meanwhile, GSEA on *in vitro*-specific modules from the second and third epochs revealed the underlying activation of neural-related programs in the *in vitro* ESC-derived mesoderm (Figures 7C and S7D). Most of the modules were enriched for neuroectoderm processes, implying that the *in vitro* differentiated cells failed to completely inhibit the default neuroectoderm lineage and instead retained a network topology capable of activating at least portions of neuroectoderm programs. This aligns with our observation that the majority of the *in vitro*-differentiated cells tended toward the neuroectoderm lineage. Our results suggest that to more efficiently produce mesodermal cells, emphasis should be placed on disrupting network module topologies responsible for neural programs.

DISCUSSION

Here, we presented a GRN reconstruction tool, Epoch, which leverages single-cell transcriptomics and efficiently infers dynamic network structures. We show that it outperforms methods designed for bulk and single-cell GRN reconstruction in both synthetically generated and real-world datasets. It is computationally efficient, facilitating

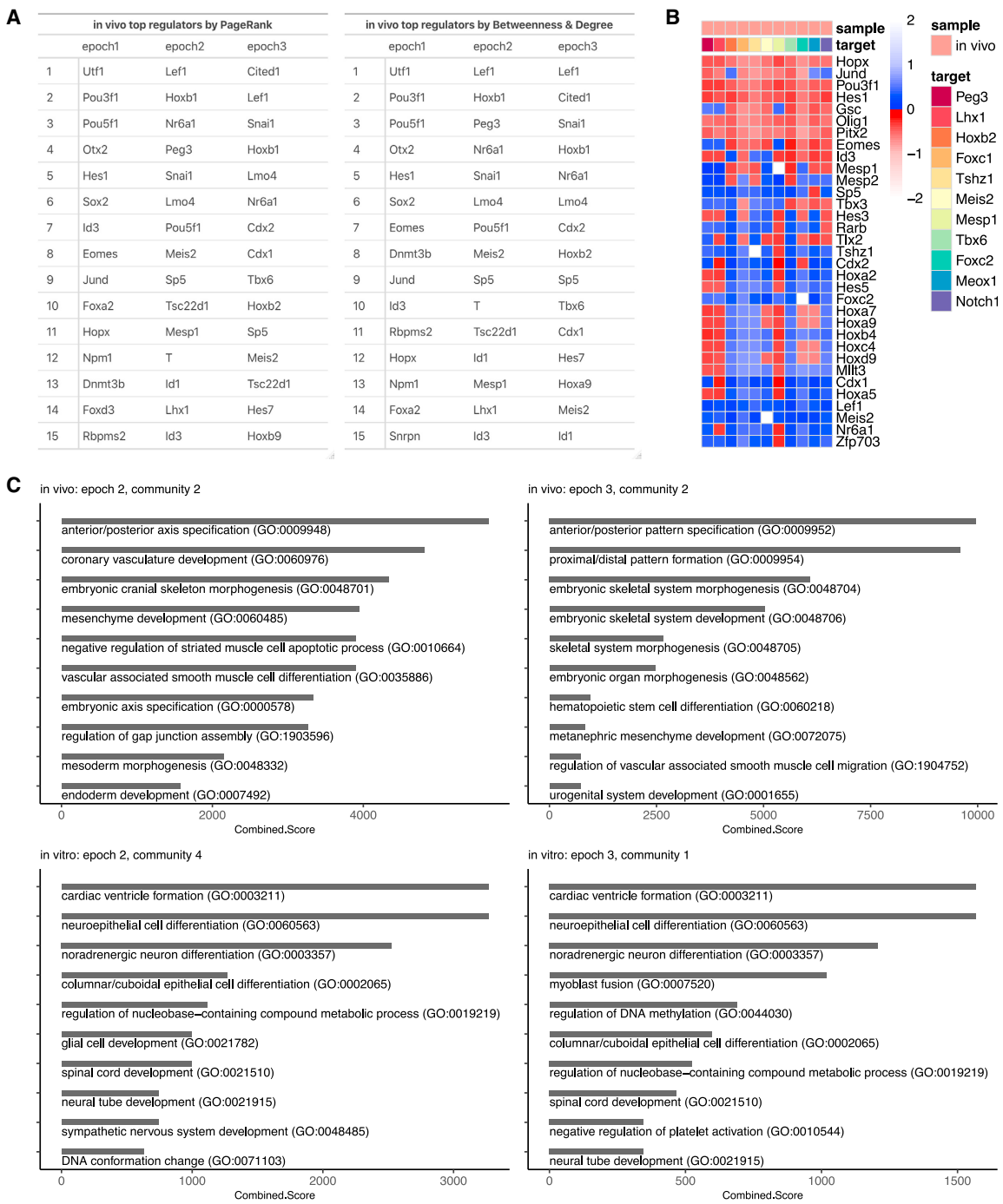

Figure 7. Comparison to *in vivo* gastrulation and mesoderm specification

(A) Top regulators of each epoch in the *in vivo* mesoderm network as predicted by PageRank and Betweenness-Degree.

(B) Shortest path analysis showing length of shortest paths from Wnt effector targets (each row) to mesodermal target genes (each column) in the *in vivo* network. Path lengths are normalized against average path length in the network. Blue and red indicate paths that activate and repress the target gene, respectively. If such a path does not exist, then it has length of infinity and is white.

(C) Top 10 enriched terms for *in vivo*- and *in vitro*-specific modules based on the Combined Score from Enrichr GSEA analysis. See also Figure S7.

the optimization of network topology or iterative simulations of changes in network structure. Finally, the utility of Epoch is enhanced by its flexibility; there are no strict requirements on the flavor of pseudotemporal input, and its workflow is structured in discrete steps, allowing users to pick and choose or substitute portions of the workflow, making it straightforward to incorporate emerging analysis techniques into the framework of Epoch.

To demonstrate the practical utility of Epoch, we applied it to scRNA-seq data from d0 through d4 in *in vitro* mESC-directed differentiation undergoing 4 treatments (WAG, WAB, WAN, and WA). This analysis revealed several topological features that are likely to play important roles in specifying germ layer fate during directed differentiation.

First, we identified a set of *Peg3*-controlled TF modules that promote mesoderm emergence, which were preferentially activated in WAG. This, coupled with prior data linking GSK3 to the regulation of imprinted genes (Meredith et al., 2015), preferential expression of *Peg3* in mesoderm and somites (Kuroiwa et al., 1996), and the inhibitory influence of *Peg3* on pluripotency and reprogramming (Theka et al., 2017), implicate *Peg3* as a candidate to improve the efficiency of directed differentiation toward mesodermal fates.

Second, by integrating Epoch-reconstructed dynamic GRNs with signaling pathways, we were able to trace paths from signaling effectors through GRNs to the regulation of germ-layer-specific gene batteries. This revealed not only direct targets of signal pathways but also broad network remodeling that altered accessibility to targets, thereby honing the capacity and potential for distinct fates. Specifically, we found that paths from Wnt signaling effectors to mesodermal programs were confined to the WAG network. Similarly, we found condition-specific paths between the suppression of PI3K signaling, subsequent *Foxo1* activation, and endoderm specification. Collectively, these analyses supported our hypothesis that signaling-induced topological differences altered the cell fate landscape, resulting in distinct propensities for each germ layer. The nature of these topological differences remains unclear. One possibility is direct alteration of the epigenomic state, and thus GRN, by signaling pathways. We point to the reported effect of GSK over *Peg3* methylation as an example of such a phenomenon. Further studies to elucidate differences in epigenomic states between mESCs undergoing directed differentiation by modulation of distinct signaling pathways will aid in clarifying whether such a mechanism is in play.

Finally, we explored how *in vivo* versus *in vitro* mesoderm specification GRNs compare, revealing two broad GRN differences. First, the *in vivo* GRN established patterning and axis-specification programs that were lacking in the *in vitro* network, consistent with incomplete recapitulation of the self-organization present in *in vivo* gastrulation (ten Berge et al., 2008; Glykofrydis et al., 2021). Second, the *in vitro* GRN retained a topology partially favorable for neuroectoderm development, suggesting that the cells undergoing *in vitro*-directed differentiation incompletely suppressed the neuroectoderm fate. Overall, this analysis suggests that guiding cells toward a more faithful mesodermal fate at a higher rate will likely require steps to disrupt the retention of neuroectoderm-favoring networks while promoting the establishment of appropriate patterning-related programs.

Our results ultimately suggest a model of differentiation that is driven by the activation of genetic programs and honed by network topology changes. In other words, signaling-induced restructuring of GRNs alters the fate potential landscape, which allows for independent control of multiple genetic programs and thereby increases the diversity of reachable cell states. In the case of mESC-directed differentiation, GRN topology clearly restricted the potential of cells toward specific fates, resulting in different propensities for mesoderm, endoderm, and neuroectoderm depending on treatment. Finally, while it may be the case that both signaling activities described (i.e., the effector regulation of distinct targets and the restructuring of network topology) occur concurrently, it is ultimately difficult to resolve their relative timing.

The methodology presented here, available in the R package Epoch, is broadly applicable to any biological question that benefits from uncovering dynamic regulatory networks, their comparisons, and their interfacing with signaling pathways. In particular, Epoch can be used to understand cell fate transitions at branch points in lineage trajectories, to uncover key regulators driving these decisions, and to trace paths from signal transduction events to the activation or repression of transcriptional programs. Such an approach provides a powerful strategy to not only elucidate dynamic, multiscale processes in development but also to identify signaling pathways to modulate for the purposes of directing cell identity transitions *in vitro*.

EXPERIMENTAL PROCEDURES

Epoch workflow

Epoch takes as input processed (normalized and log-transformed) single-cell transcriptomic data and accompanying pseudotime (or equivalent) annotation. The Epoch workflow is based on three strategies: (1) the extraction of dynamically expressed genes and subsequent static reconstruction with CLR, (2) network refinement using a cross-correlation based strategy called cross-weighting, and (3) the extraction of a dynamic network and the subsequent identification of top regulators.

Identification of dynamically expressed genes

Limiting network reconstruction to dynamically expressed genes serves two purposes. First, it focuses the network on interactions that more likely play a role in the observed biological process.

Second, it reduces the instances of false positive interactions and improves precision by limiting possible edges between temporally variable genes. To select for such genes, Epoch models individual genes across the annotated pseudotime using a generalized additive model (GAM). Specifically, Epoch uses the 'gam' package (Gaussian family, LOESS smooth pseudotime) to fit a model for each gene using the backfitting algorithm. Genes are considered dynamic based on the significance of the smooth term (pseudotime). Alternatively, users can specify finding dynamic genes via TradeSeq (Van den Berge et al., 2020), a recently developed tool that identifies dynamic changes in gene expression via a GAM based on the negative binomial distribution.

Cross-weighting

After inferring an initial network structure, Epoch can apply cross-weighting. The objective of this step is to negatively weight edges in the initial network that are unlikely to be true interactions, which may, for example, be representative of indirect interactions. To this end, for every TF-target pair in the initial network, Epoch computes cross-correlation across a given lag time (defaults to one-fifth of total pseudotime). After ordering the lag times by decreasing correlation, Epoch computes an offset value in which maximum correlation is achieved, defined by default as the top one-third of the ranked lag times. Finally, Epoch scores the offset values of each interaction:

$$weight = \begin{cases} 1 & x \leq w_{min} \\ 0 & x \geq w_{max} \\ -x/(w_{max} - w_{min}) + 1 & else \end{cases}$$

where the offset, x, is computed as described, and maximum and minimum windows can be altered by the user if desired. Z-scores from the initial network are weighted accordingly, ultimately filtering out false positives. At this step, Epoch will return an appended GRN table, including the offset value and new weighted score for each interaction.

Default parameters for cross-weighting are specified within Epoch, and were chosen based on empirical improvements in performance across synthetic and real datasets (ranging in number of genes, number of cells, and simple trajectory types). For example, we found that optimal lag time varied to some extent with dataset size, with larger datasets requiring a larger lag time to catch target response to regulator expression changes (Figure S1E). Smaller lag times tended to correlate with decreased AUPR, likely because the lag time was not sufficient to catch the point of maximum cross-correlation. AUPR also begins to gradually decrease at larger lag times, although this effect is much less pronounced. We found that our default lag (set to one-fifth of the dataset size) resulted in high AUPR across various datasets. Similarly, we also examined various minimum and maximum windows and found that our default values resulted in optimal AUPR (Figure S1F) across datasets of varying sizes. However, users may want to modify these parameters to increase or decrease the leniency of the weighting for a number of reasons, such as when applying Epoch to more complex trajectories with large numbers or more complex state changes (and, correspondingly, a large number of epochs). In this case, we would recommend finding optimal lag and window in an analogous method. Specifically, this would entail designing a modular network (and corresponding GRN) representative of the more complex trajectory, using this network to simulate synthetic datasets, and performing a parameter sweep to optimize reconstruction AUPR. Synthetic network design and simulation for both simple and complex trajectories can be done via platforms such as Dyngen (Cannoodt et al., 2021).

Dynamic network extraction

Epoch will extract a dynamic network from the reconstructed static network. Specifically, the process begins by breaking pseudotime into epochs. A number of options are available to users to accomplish this. Briefly, Epoch can define the epochs based on pseudotime, equal cell ordering (resulting in equal number of cells per epoch), k-means or hierarchical clustering, sliding window similarity, or user-defined manual assignment. With the exception of user-defined assignment and sliding window similarity, the number of epochs is specified by the user, and can be determined by examining the heatmap of gene expression across pseudotime and estimating the rough number of expression states represented in the data. We recommend smoothing the data to aid in heatmap visualization, which can be done through Epoch. Alternatively, it is unnecessary to supply the number of epochs if using the similarity method, which will automatically detect epochs based on correlation between groups of cells along a sliding window across pseudotime. After epochs are defined, Epoch will assign genes to epochs, based on their activity along pseudotime. In brief, this is either based on activity (i.e., genes active in any epochs will be assigned to those epochs) or on differential expression (i.e., genes are assigned based on whether they are differentially expressed in an epoch). Specifically, if genes are assigned by activity, Epoch will compute, for each gene, a threshold against which average expression of the gene in an epoch is compared. This threshold can be modified by user input. If, instead, genes are assigned by differential expression, a p-value threshold is used to determine assignments. Finally, "orphan genes," which we define as dynamically expressed genes that are not assigned to any epoch, are assigned to the epoch in which their average expression is maximum.

Based on these assignments, Epoch will fracture the static network into a dynamic one composed of epoch networks and transition networks. Specifically, an edge between regulator and target gene appears in an epoch network if the regulator is assigned to that epoch. Furthermore, an edge will appear in a transition subnetwork under two conditions: (1) For an activating edge, the target is not active in the source epoch, the target is active in the subsequent epoch, and the regulator is active, or (2) for a repressive edge, the target is active in the source epoch, is not active in the subsequent epoch, and the regulator is active. Following this step, Epoch will return a dynamic network represented by a list of individual GRN tables. This includes the epoch networks or essentially the dynamic network, as well as transition networks that describe how an epoch network may transition into a subsequent epoch network.

Top regulator prediction

Epoch uses two graph theoretic methods to predict the "top regulators," the TFs that appear to have the most influence in driving changes in or maintaining topology. First, Epoch will rank

regulators by weighted PageRank. In brief, the PageRank centrality measures the importance of nodes in a network based on the number and quality of links of which a node is a part. In essence, the most influential nodes are likely to interact with many influential nodes. Second, Epoch will rank regulators by the product of normalized betweenness and normalized degree. Here, the assumption is that the most influential nodes are likely to be traversed by many shortest paths (and thus have high betweenness) and interact with many other nodes (and thus have high degree). In Epoch, PageRank, betweenness, and degree centralities are implemented through the 'igraph' package. By default, cross-weighted edge weights are used, but can be further specified by the user. In both top regulator prediction methods, Epoch will return ranked lists of nodes and further specify their corresponding PageRank or normalized betweenness, normalized degree, and betweenness-degree product.

Data and code availability

Epoch is available as a package in R, and code and tutorials can be found at https://github.com/pcahan1/epoch. Data are available at GEO under accession number GEO: GSE177051.

SUPPLEMENTAL INFORMATION

Supplemental information can be found online at https://doi.org/10.1016/j.stemcr.2021.12.018.

AUTHOR CONTRIBUTIONS

E.Y.S. and P.C. developed Epoch with assistance from J.Y.K., performed analysis, and wrote the manuscript. A.S. performed *in vitro* differentiation experiments with the assistance of E.Y.S. Q.B. performed the mouse muscle development experiments. P.C. conceptualized and supervised the project.

CONFLICTS OF INTEREST

The authors declare no competing interests.

ACKNOWLEDGMENTS

We would like to thank Yuqi Tan, Ray Cheng, Eric Kernfeld, and David Johanson. We also thank Chris McGinnis for help with the MULTI-seq protocol and associated reagents. This work was supported by the NIH under grant R35GM124725 to P.C. and by the NSF Graduate Research Fellowship under grant no. DGE-1746891 to E.Y.S.

Received: November 18, 2021
Revised: December 21, 2021
Accepted: December 26, 2021
Published: January 27, 2022

REFERENCES

Aibar, S., González-Blas, C.B., Moerman, T., Huynh-Thu, V.A., Imrichova, H., Hulselmans, G., Rambow, F., Marine, J.-C., Geurts, P., Aerts, J., et al. (2017). SCENIC: single-cell regulatory network inference and clustering. Nat. Methods *14*, 1083–1086.

Androutsellis-Theotokis, A., Leker, R.R., Soldner, F., Hoeppner, D.J., Ravin, R., Poser, S.W., Rueger, M.A., Bae, S.-K., Kittappa, R., and McKay, R.D.G. (2006). Notch signalling regulates stem cell numbers in vitro and in vivo. Nature *442*, 823–826.

Aubert, J., Dunstan, H., Chambers, I., and Smith, A. (2002). Functional gene screening in embryonic stem cells implicates Wnt antagonism in neural differentiation. Nat. Biotechnol. *20*, 1240–1245.

ten Berge, D., Koole, W., Fuerer, C., Fish, M., Eroglu, E., and Nusse, R. (2008). Wnt signaling mediates self-organization and axis formation in embryoid bodies. Cell Stem Cell *3*, 508–518.

Van den Berge, K., Roux de Bézieux, H., Street, K., Saelens, W., Cannoodt, R., Saeys, Y., Dudoit, S., and Clement, L. (2020). Trajectory-based differential expression analysis for single-cell sequencing data. Nat. Commun. *11*, 1201.

Bergen, V., Lange, M., Peidli, S., Wolf, F.A., and Theis, F.J. (2020). Generalizing RNA velocity to transient cell states through dynamical modeling. Nat. Biotechnol. *38*, 1408–1414.

di Bernardo, D., Thompson, M.J., Gardner, T.S., Chobot, S.E., Eastwood, E.L., Wojtovich, A.P., Elliott, S.J., Schaus, S.E., and Collins, J.J. (2005). Chemogenomic profiling on a genome-wide scale using reverse-engineered gene networks. Nat. Biotechnol. *23*, 377–383.

Bonnaffoux, A., Herbach, U., Richard, A., Guillemin, A., Gonin-Giraud, S., Gros, P.-A., and Gandrillon, O. (2019). WASABI: a dynamic iterative framework for gene regulatory network inference. BMC Bioinformatics *20*, 220.

Brin, S., and Page, L. (1998). The anatomy of a large-scale hypertextual web search engine. Computer Networks ISDN Syst. *30*, 107–117.

Buenrostro, J.D., Giresi, P.G., Zaba, L.C., Chang, H.Y., and Greenleaf, W.J. (2013). Transposition of native chromatin for fast and sensitive epigenomic profiling of open chromatin, DNA-binding proteins and nucleosome position. Nat. Methods *10*, 1213–1218.

Cahan, P., Cacchiarelli, D., Dunn, S.-J., Hemberg, M., de Sousa Lopes, S.M.C., Morris, S.A., Rackham, O.J.L., Del Sol, A., and Wells, C.A. (2021). Computational stem cell biology: open questions and guiding principles. Cell Stem Cell *28*, 20–32.

Cannoodt, R., Saelens, W., Deconinck, L., and Saeys, Y. (2021). Spearheading future omics analyses using dyngen, a multi-modal simulator of single cells. Nat. Commun. *12*, 3942.

Carro, M.S., Lim, W.K., Alvarez, M.J., Bollo, R.J., Zhao, X., Snyder, E.Y., Sulman, E.P., Anne, S.L., Doetsch, F., Colman, H., et al. (2010). The transcriptional network for mesenchymal transformation of brain tumours. Nature *463*, 318–325.

Chen, S., and Mar, J.C. (2018). Evaluating methods of inferring gene regulatory networks highlights their lack of performance for single cell gene expression data. BMC Bioinformatics *19*, 232.

Davidson, E.H., and Erwin, D.H. (2006). Gene regulatory networks and the evolution of animal body plans. Science *311*, 796–800.

Dunn, S.J., Martello, G., Yordanov, B., Emmott, S., and Smith, A.G. (2014). Defining an essential transcription factor program for naïve pluripotency. Science *344*, 1156–1160.

Faith, J.J., Hayete, B., Thaden, J.T., Mogno, I., Wierzbowski, J., Cottarel, G., Kasif, S., Collins, J.J., and Gardner, T.S. (2007). Large-scale

mapping and validation of Escherichia coli transcriptional regulation from a compendium of expression profiles. PLoS Biol. *5*, e8.

Genga, R.M.J., Kernfeld, E.M., Parsi, K.M., Parsons, T.J., Ziller, M.J., and Maehr, R. (2019). Single-cell RNA-sequencing-based CRISPRi screening resolves molecular drivers of early human endoderm development. Cell Rep. *27*, 708–718.e10.

Glykofrydis, F., Cachat, E., Berzanskyte, I., Dzierzak, E., and Davies, J.A. (2021). Bioengineering self-organizing signaling centers to control embryoid body pattern elaboration. ACS Synth. Biol. *10*, 1465–1480.

Grosswendt, S., Kretzmer, H., Smith, Z.D., Kumar, A.S., Hetzel, S., Wittler, L., Klages, S., Timmermann, B., Mukherji, S., and Meissner, A. (2020). Epigenetic regulator function through mouse gastrulation. Nature *584*, 102–108.

Haghverdi, L., Büttner, M., Wolf, F.A., Buettner, F., and Theis, F.J. (2016). Diffusion pseudotime robustly reconstructs lineage branching. Nat. Methods *13*, 845–848.

Hartemink, A.J. (2005). Reverse engineering gene regulatory networks. Nat. Biotechnol. *23*, 554–555.

Huynh-Thu, V.A., Irrthum, A., Wehenkel, L., and Geurts, P. (2010). Inferring regulatory networks from expression data using tree-based methods. PLoS One *5*, e12776.

Karlebach, G., and Shamir, R. (2008). Modelling and analysis of gene regulatory networks. Nat. Rev. Mol. Cell Biol. *9*, 770–780.

Klein, A.M., Mazutis, L., Akartuna, I., Tallapragada, N., Veres, A., Li, V., Peshkin, L., Weitz, D.A., and Kirschner, M.W. (2015). Droplet barcoding for single-cell transcriptomics applied to embryonic stem cells. Cell *161*, 1187–1201.

Kuroiwa, Y., Kaneko-Ishino, T., Kagitani, F., Kohda, T., Li, L.L., Tada, M., Suzuki, R., Yokoyama, M., Shiroishi, T., Wakana, S., et al. (1996). Peg3 imprinted gene on proximal chromosome 7 encodes for a zinc finger protein. Nat. Genet. *12*, 186–190.

Letsou, W., and Cai, L. (2016). Noncommutative biology: sequential regulation of complex networks. PLoS Comput. Biol. *12*, e1005089.

Macosko, E.Z., Basu, A., Satija, R., Nemesh, J., Shekhar, K., Goldman, M., Tirosh, I., Bialas, A.R., Kamitaki, N., Martersteck, E.M., et al. (2015). Highly parallel genome-wide expression profiling of individual cells using nanoliter droplets. Cell *161*, 1202–1214.

La Manno, G., Soldatov, R., Zeisel, A., Braun, E., Hochgerner, H., Petukhov, V., Lidschreiber, K., Kastriti, M.E., Lönnerberg, P., Furlan, A., et al. (2018). RNA velocity of single cells. Nature *560*, 494–498.

Marbach, D., Prill, R.J., Schaffter, T., Mattiussi, C., Floreano, D., and Stolovitzky, G. (2010). Revealing strengths and weaknesses of methods for gene network inference. Proc. Natl. Acad. Sci. U S A *107*, 6286–6291.

Marbach, D., Costello, J.C., Küffner, R., Vega, N.M., Prill, R.J., Camacho, D.M., Allison, K.R., DREAM5 Consortium, Kellis, M., Collins, J.J., et al. (2012). Wisdom of crowds for robust gene network inference. Nat. Methods *9*, 796–804.

Margolin, A.A., Nemenman, I., Basso, K., Wiggins, C., Stolovitzky, G., Dalla Favera, R., and Califano, A. (2006). ARACNE: an algorithm for the reconstruction of gene regulatory networks in a mammalian cellular context. BMC Bioinformatics *7* (*Suppl 1*), S7.

Matsumoto, H., Kiryu, H., Furusawa, C., Ko, M.S.H., Ko, S.B.H., Gouda, N., Hayashi, T., and Nikaido, I. (2017). SCODE: an efficient regulatory network inference algorithm from single-cell RNA-Seq during differentiation. Bioinformatics *33*, 2314–2321.

McGinnis, C.S., Patterson, D.M., Winkler, J., Conrad, D.N., Hein, M.Y., Srivastava, V., Hu, J.L., Murrow, L.M., Weissman, J.S., Werb, Z., et al. (2019). MULTI-seq: sample multiplexing for single-cell RNA sequencing using lipid-tagged indices. Nat. Methods *16*, 619–626.

McLean, A.B., D'Amour, K.A., Jones, K.L., Krishnamoorthy, M., Kulik, M.J., Reynolds, D.M., Sheppard, A.M., Liu, H., Xu, Y., Baetge, E.E., et al. (2007). Activin a efficiently specifies definitive endoderm from human embryonic stem cells only when phosphatidylinositol 3-kinase signaling is suppressed. Stem Cells *25*, 29–38.

Meredith, G.D., D'Ippolito, A., Dudas, M., Zeidner, L.C., Hostetter, L., Faulds, K., Arnold, T.H., Popkie, A.P., Doble, B.W., Marnellos, G., et al. (2015). Glycogen synthase kinase-3 (Gsk-3) plays a fundamental role in maintaining DNA methylation at imprinted loci in mouse embryonic stem cells. Mol. Biol. Cell *26*, 2139–2150.

Meyer, P.E., Kontos, K., Lafitte, F., and Bontempi, G. (2007). Information-theoretic inference of large transcriptional regulatory networks. EURASIP J. Bioinform. Syst. Biol. *2007*, 79879.

Morgan, D., Studham, M., Tjärnberg, A., Weishaupt, H., Swartling, F.J., Nordling, T.E.M., and Sonnhammer, E.L.L. (2020). Perturbation-based gene regulatory network inference to unravel oncogenic mechanisms. Sci. Rep. *10*, 14149.

Nord, J., Schill, D., Pulakanti, K., Rao, S., and Cirillo, L.A. (2020). The transcription factor FoxO1 is required for the establishment of the human definitive endoderm. BioRxiv https://doi.org/10.1101/2020.12.22.423976.

Le Novère, N. (2015). Quantitative and logic modelling of molecular and gene networks. Nat. Rev. Genet. *16*, 146–158.

Popkie, A.P., Zeidner, L.C., Albrecht, A.M., D'Ippolito, A., Eckardt, S., Newsom, D.E., Groden, J., Doble, B.W., Aronow, B., McLaughlin, K.J., et al. (2010). Phosphatidylinositol 3-kinase (PI3K) signaling via glycogen synthase kinase-3 (Gsk-3) regulates DNA methylation of imprinted loci. J. Biol. Chem. *285*, 41337–41347.

Pratapa, A., Jalihal, A.P., Law, J.N., Bharadwaj, A., and Murali, T.M. (2020). Benchmarking algorithms for gene regulatory network inference from single-cell transcriptomic data. Nat. Methods *17*, 147–154.

Qin, G., Yang, L., Ma, Y., Liu, J., and Huo, Q. (2019). The exploration of disease-specific gene regulatory networks in esophageal carcinoma and stomach adenocarcinoma. BMC Bioinformatics *20*, 717.

Qiu, P., Simonds, E.F., Bendall, S.C., Gibbs, K.D., Bruggner, R.V., Linderman, M.D., Sachs, K., Nolan, G.P., and Plevritis, S.K. (2011). Extracting a cellular hierarchy from high-dimensional cytometry data with SPADE. Nat. Biotechnol. *29*, 886–891.

Qiu, X., Rahimzamani, A., Wang, L., Ren, B., Mao, Q., Durham, T., McFaline-Figueroa, J.L., Saunders, L., Trapnell, C., and Kannan, S. (2020). Inferring causal gene regulatory networks from coupled

single-cell expression dynamics using scribe. Cell Syst *10*, 265–274.e11.

Rackham, O.J.L., Firas, J., Fang, H., Oates, M.E., Holmes, M.L., Knaupp, A.S., FANTOM Consortium, Suzuki, H., Nefzger, C.M., Daub, C.O., et al. (2016). A predictive computational framework for direct reprogramming between human cell types. Nat. Genet. *48*, 331–335.

Stark, J., Brewer, D., Barenco, M., Tomescu, D., Callard, R., and Hubank, M. (2003). Reconstructing gene networks: what are the limits? Biochem. Soc. Trans. *31*, 1519–1525.

Street, K., Risso, D., Fletcher, R.B., Das, D., Ngai, J., Yosef, N., Purdom, E., and Dudoit, S. (2018). Slingshot: cell lineage and pseudotime inference for single-cell transcriptomics. BMC Genomics *19*, 477.

Tan, Y., and Cahan, P. (2019). SingleCellNet: a computational tool to classify single cell RNA-seq data across platforms and across species. Cell Syst. *9*, 207–213.e2.

Theka, I., Sottile, F., Aulicino, F., Garcia, A.C., and Cosma, M.P. (2017). Reduced expression of Paternally Expressed Gene-3 enhances somatic cell reprogramming through mitochondrial activity perturbation. Sci. Rep. *7*, 9705.

Trapnell, C. (2015). Defining cell types and states with single-cell genomics. Genome Res. *25*, 1491–1498.

Trapnell, C., Cacchiarelli, D., Grimsby, J., Pokharel, P., Li, S., Morse, M., Lennon, N.J., Livak, K.J., Mikkelsen, T.S., and Rinn, J.L. (2014). The dynamics and regulators of cell fate decisions are revealed by pseudotemporal ordering of single cells. Nat. Biotechnol. *32*, 381–386.

Wolf, F.A., Angerer, P., and Theis, F.J. (2018). SCANPY: large-scale single-cell gene expression data analysis. Genome Biol. *19*, 15.

Yu, J., Smith, V.A., Wang, P.P., Hartemink, A.J., and Jarvis, E.D. (2004). Advances to Bayesian network inference for generating causal networks from observational biological data. Bioinformatics *20*, 3594–3603.

Yu, J.S.L., Ramasamy, T.S., Murphy, N., Holt, M.K., Czapiewski, R., Wei, S.-K., and Cui, W. (2015). PI3K/mTORC2 regulates TGF-β/Activin signalling by modulating Smad2/3 activity via linker phosphorylation. Nat. Commun. *6*, 7212.

Zheng, G.X.Y., Terry, J.M., Belgrader, P., Ryvkin, P., Bent, Z.W., Wilson, R., Ziraldo, S.B., Wheeler, T.D., McDermott, G.P., Zhu, J., et al. (2017). Massively parallel digital transcriptional profiling of single cells. Nat. Commun. *8*, 14049.

Stem Cell Reports, Volume *17*

Supplemental Information

Reconstruction of dynamic regulatory networks reveals signaling-induced topology changes associated with germ layer specification

Emily Y. Su, Abby Spangler, Qin Bian, Jessica Y. Kasamoto, and Patrick Cahan

Supplemental Items

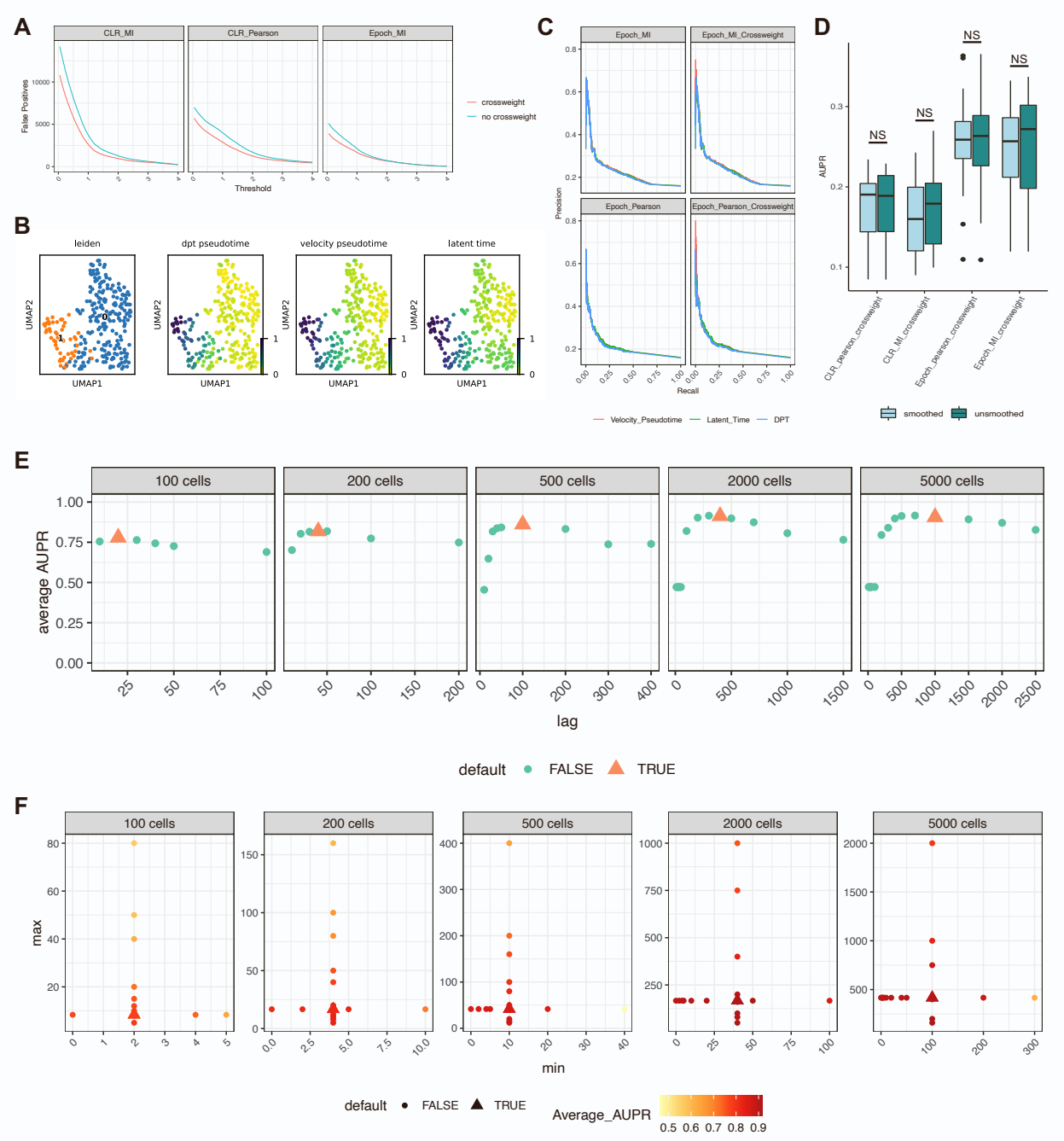

Figure S1. The effect of cross-weighting, TI method, smoothing, and parameter choices on performance.
(A) An example from GRN reconstruction on a synthetic dataset showing the difference in number of false positives based on whether or not cross-weighting is performed. See Note S1 for information on synthetic dataset. (B) Clustering, diffusion pseudotime, velocity pseudotime, and latent time of the E12.5 muscle development data. See Note S1 for dataset details. (C) Precision recall curves of four variations of Epoch using three different pseudotime annotations on the E12.5 muscle development data. There was no clear difference in performance based on pseudotime method used. (D) Effect of smoothing vs. no smoothing on AUPR of reconstruction using various methods. There was no significant difference in performance between using kernel-smoothed data and unsmoothed data. Smoothing functions remain in Epoch's code

to aid in cleaner visualizations of gene dynamics. (E) Average AUPR of reconstruction using different cross-weighting lag times across datasets of varying sizes, taken from BEELINE linear datasets. Each dataset size contains 10 distinct datasets, Default lag time is plotted as the orange triangle, and is computed as one-fifth of the number of cells in the data. (F) Average AUPR of reconstruction using different minimum and maximum windows in cross-weighting. Data shown is reconstruction from BEELINE linear datasets. Each dataset size contains 10 distinct datasets. Default minimum and maximum is indicated by the triangle, and is defined as 1/50 and 1/12 of total cells respectively. High average AUPR is indicated by the darker red colors.

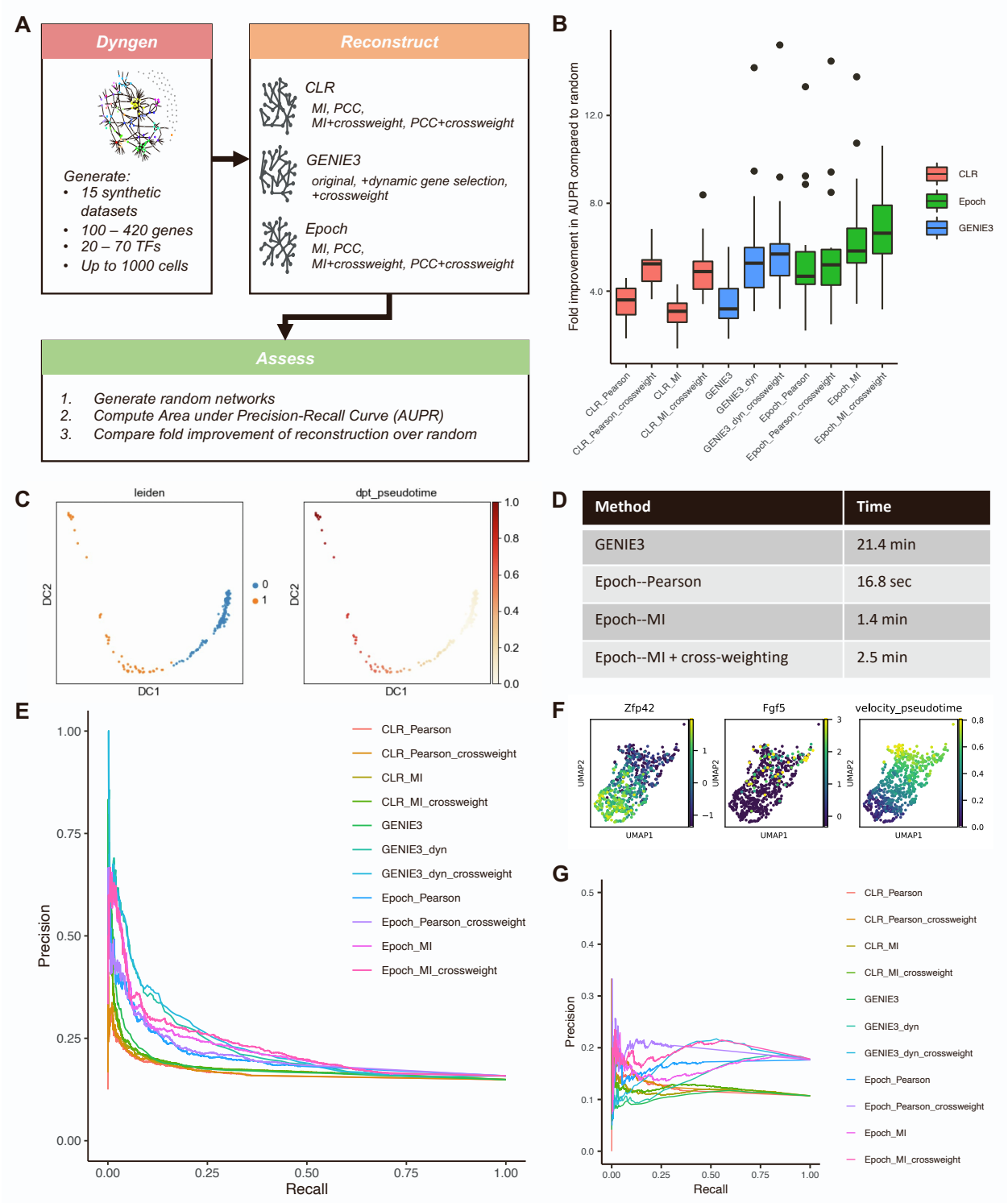

Figure S2. Epoch benchmarking, related to Note S1.
(A) Synthetic dataset generation via Dyngen, reconstruction, and assessment. (B) Full results of benchmarking reconstruction of synthetic data. Four versions of CLR (Pearson vs. MI, cross-weighting vs. no cross-weighting), four versions of Epoch (same as CLR), and three versions of GENIE3 (original, limited to dynamic genes, and with cross-weighting) are compared. Kruskal-Wallis $p=1.75 \times 10^{-11}$. (C) Clustering and diffusion pseudotime for E12.5 muscle development data used in benchmarking. (D) Runtimes for reconstruction on muscle development data. (Runtimes were measured on a MacBook Pro

laptop with 2.9 GHz Intel Core i7 processor, 16GB 2133 MHz DDR3 of RAM). (E) Full results of benchmarking reconstruction of the muscle development data. (F) Early mESC directed differentiation data (subsetted from Spangler et al. 2018). Zfp42 expression, Fgf5 expression, and velocity pseudotime are shown. (G) Full results of benchmarking reconstruction of the early Spangler et al. data.

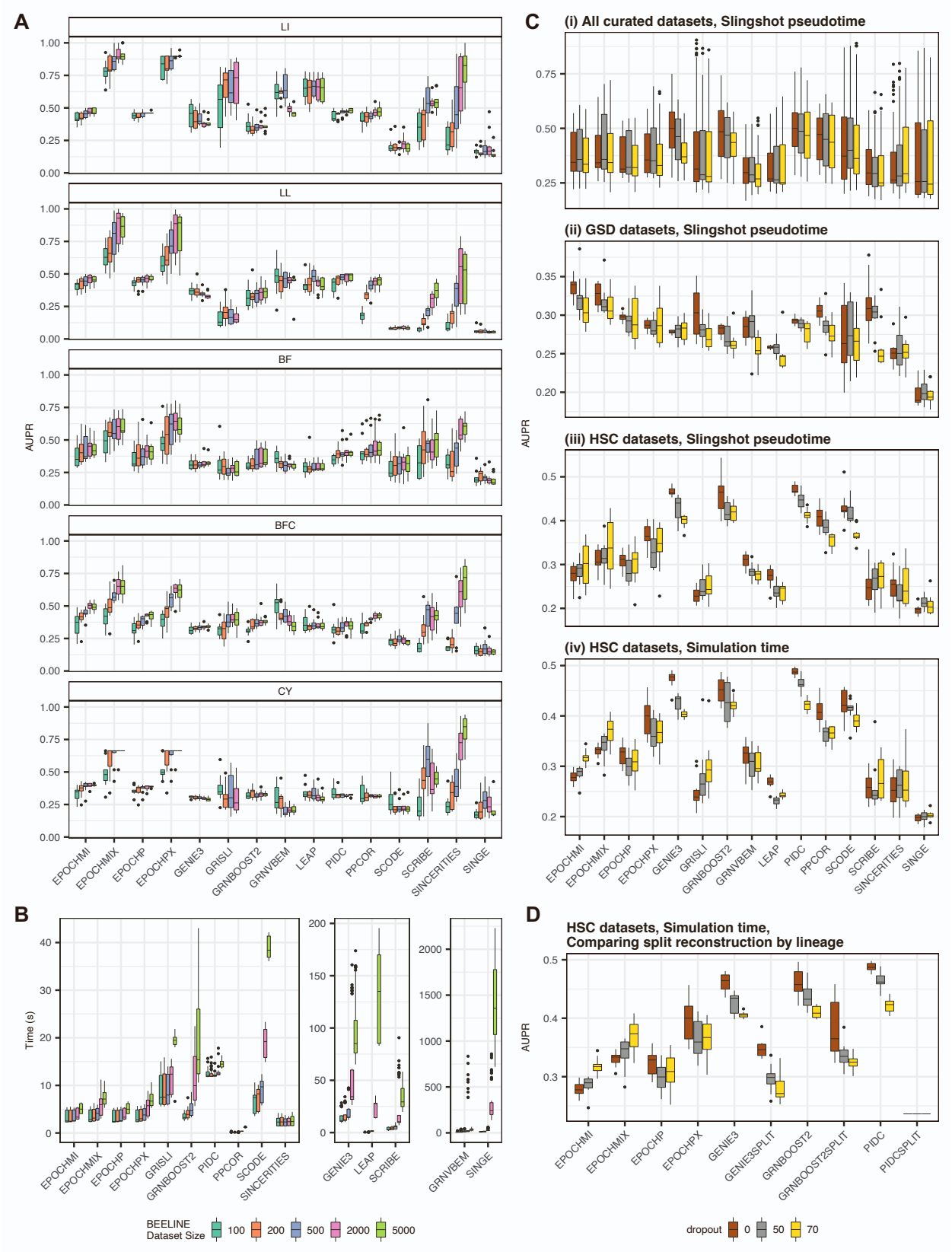

Figure S3. BEELINE data benchmarking, related to Figure 2 and Note S1.
(A) AUPR of reconstruction on synthetic data using the four versions of Epoch (MI = mutual information, P

= Pearson correlation, X = with cross-weighting) and 11 other single-cell GRN reconstruction tools. Results are faceted by trajectory type (LI = linear, LL = long linear, BF = bifurcating, BFC = bifurcating converging, CY = cycle) and colored by number of cells in the dataset. (B) BEELINE synthetic data runtimes. Runtimes (in seconds) are plotted for each method, faceted by magnitude of runtime. Four versions of Epoch are shown (MI = mutual information, P = Pearson correlation, X = with cross-weighting), along with 11 other single-cell GRN reconstruction tools. Data is colored based on number of cells in the dataset. (C) AUPR of reconstruction on curated data (as described in Pratapa et al. 2020), using the four versions of Epoch (MI = mutual information, P = Pearson correlation, X = with cross-weighting) and 11 other single-cell GRN reconstruction tools. Panel (i) summarizes the results from all curated datasets. Panel (ii) shows results from reconstruction on the GSD datasets using BEELINE-provided Slingshot pseudotime. Panel (iii) shows results from reconstruction on the HSC datasets using BEELINE-provided Slingshot pseudotime. Panel (iv) shows results from reconstruction on re-simulated HSC datasets using true simulation time from BoolODE (Pratapa et al., 2020). (D) The results from reconstruction on re-simulated HSC datasets using true simulation time, comparing the results of reconstructing using GENIE3, GRNBoost2, and PIDC with no splitting vs. splitting along each lineage before compiling (SPLIT = with splitting and compiling).

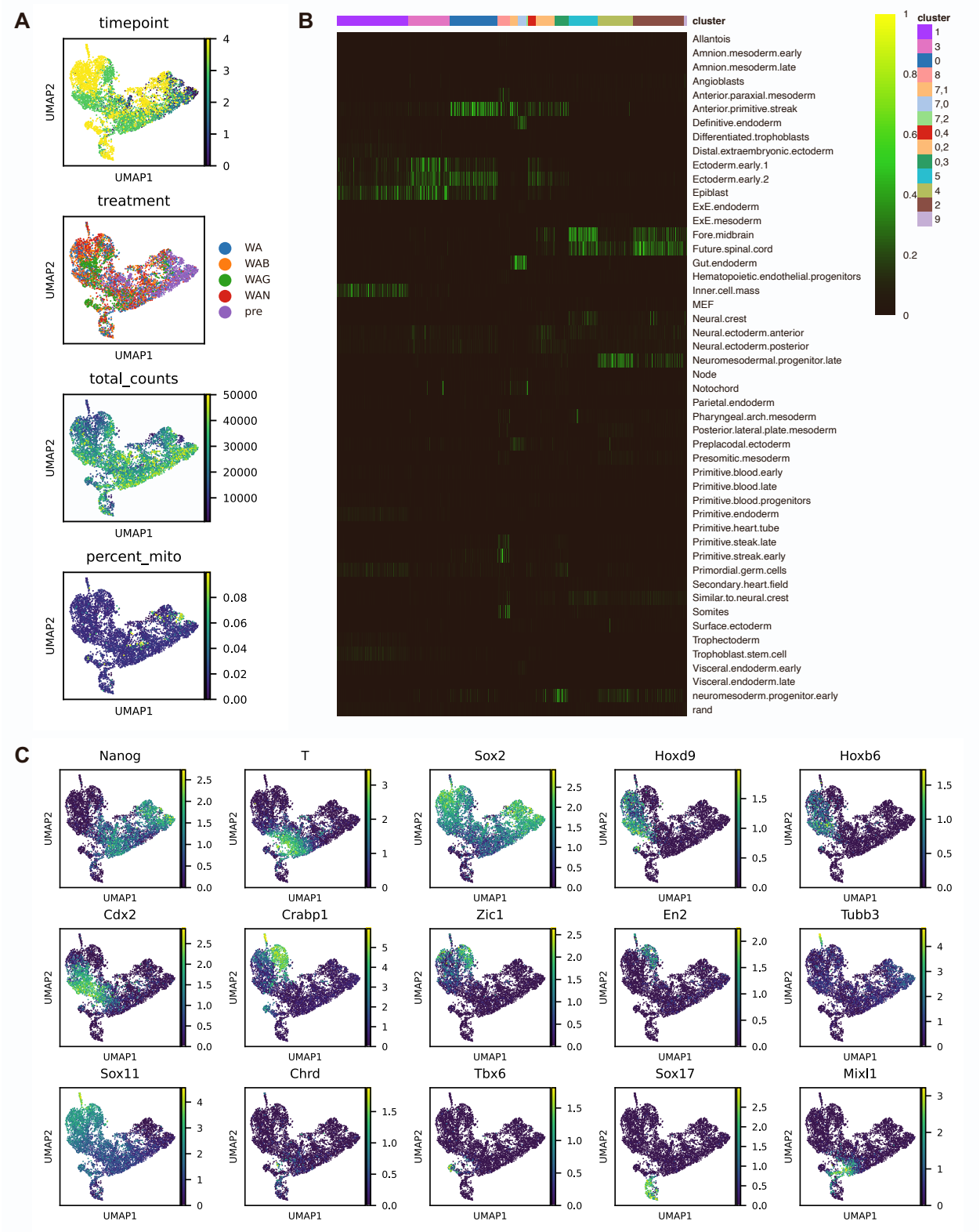

Figure S4. mESC directed differentiation cell annotations, related to Figure 3, Note S2, Table S1. (A) timepoint, treatment, total counts, and percent mitochondrial transcripts content of the MULTI-seq data. (B) SingleCellNet classification results. The classifier was trained from mouse embryo data found in literature, curated by members in the lab. (C) Select marker gene expression of the MULTI-seq data.

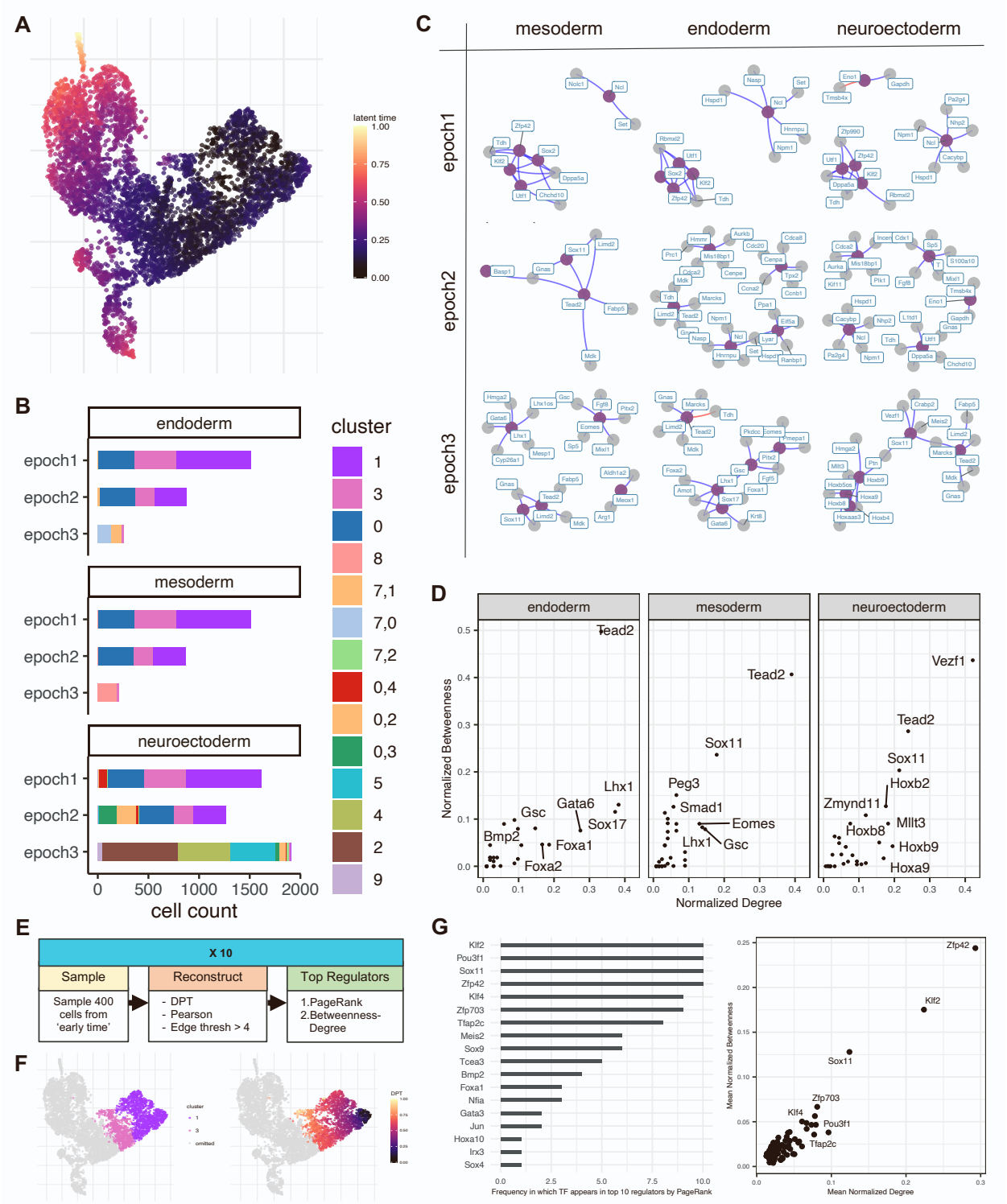

Figure S5. *in vitro* directed differentiation network reconstruction, related to Note S3.
(A) Latent time annotation for MULTI-seq data. (B) Population breakdown by cluster of epoch assignment along each germ layer path. (C) Reconstructed dynamic networks along mesoderm, endoderm, and neuroectoderm paths, with top 5 regulators colored purple and their top targets in gray as determined by PageRank. (D) Top regulators as predicted by Epoch via betweenness and degree for the third epochs along each germ layer path. (E) Workflow for bootstrapped top regulator prediction for inner cell mass to

epiblast-like transition. (F) Only cells from early time were used in this early bootstrap analysis. Clusters used and corresponding diffusion pseudotime shown here. (G) Top regulators for this early fate transition as predicted using frequency a TF scores as a top regulator by PageRank and using mean Betweenness-Degree.

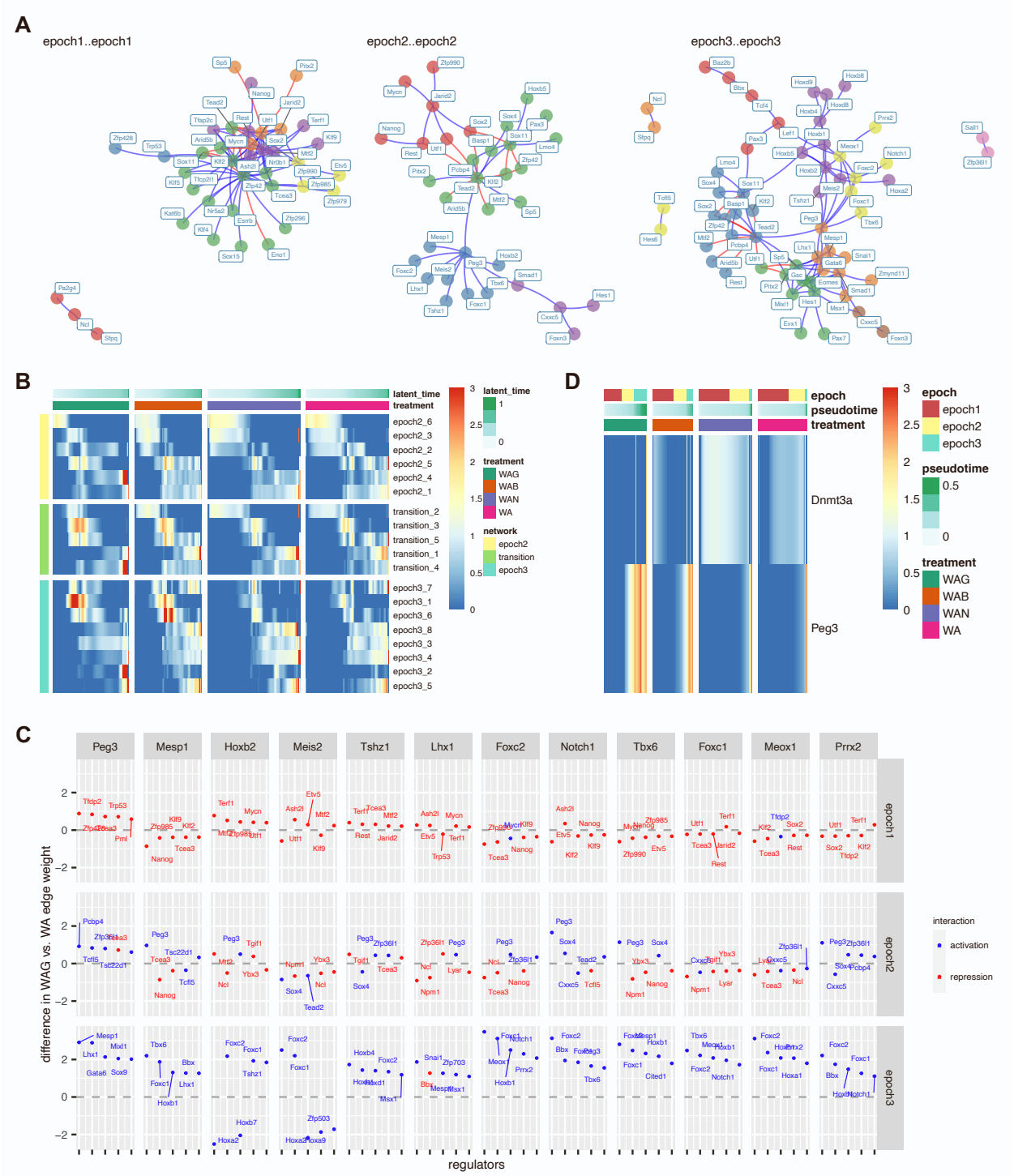

Figure S6. Mesodermal network analysis continued, related to Figure 4 and results section "*Peg3* is a central regulator in mesodermal WAG networks".

(A) Full dynamic mesodermal network. TFs are colored by community. Blue and red edges represent activating and repressive edges respectively. (B) Average community expression over time by treatment along the full dataset. Communities shown (each row) are from the epoch 2 subnetwork (yellow), transition (green), and epoch 3 subnetworks (aqua) of the mesodermal network. (C) Top differential regulators of mesodermal genes. Blue and red represent activators and repressors respectively. Y-axis is plotting difference in edge weights between the WAG and WA networks. Thus, TFs appearing above the

0-line represent interactions that are more unique to the WAG network, and those below are more unique to the WA network. (D) *Peg3* and *Dnmt3a* expression across time along the mesodermal path of the MULTI-seq data.

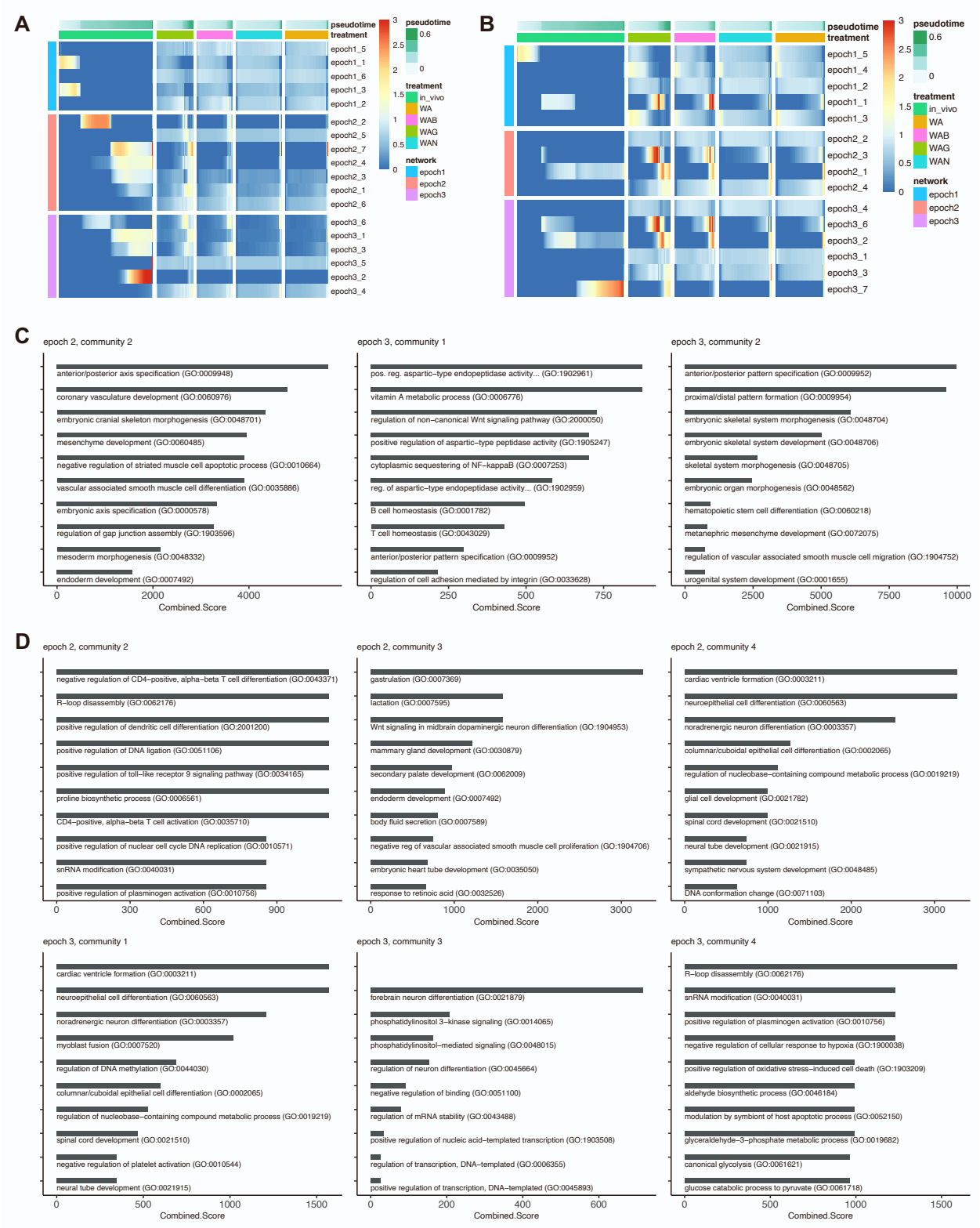

Figure S7. *In vivo* vs. *in vitro* mesodermal network comparison continued, related to Figure 7. (A) Average *in vivo* community expression over time along the mesodermal path for the *in vivo*, *in vitro* WAG, *in vitro* WAB, *in vitro* WAN, and *in vitro* WA data. (B) Average *in vitro* community expression over time along the mesodermal path for the *in vivo*, *in vitro* WAG, *in vitro* WAB, *in vitro* WAN, and *in vitro* WA

data. (C) Top ten enriched terms for *in vivo*-specific modules based on the Combined Score from Enrichr GSEA analysis. The three modules included are activated in the *in vivo* data but not (or weakly activated) in the *in vitro* data (see panel A). (D) Top ten enriched terms for *in vitro*-specific modules based on the Combined Score from Enrichr GSEA analysis. The six modules included are activated in the *in vitro* data but not (or weakly activated) in the *in vivo* data (see panel B).

Table S1. Cell type annotation by cluster of mESC directed differentiation data, related to Figure 3, S4, and Note S2.

Cluster	Cell Type Label	Evidence
1	Undifferentiated ESCs	This cluster classifies strongly as inner cell mass and epiblast. It expresses a number of pluripotency genes including *Zfp42*.
3	Epiblast	This cluster classifies as epiblast with some early ectodermal signature. *Fgf5* expression begins here.
0	Primitive Streak	This cluster classifies strongly as primitive streak with some early ectodermal signature. It expresses *Brachyury*.
8	(mesoderm) Presomitic Mesoderm/Somites	This cluster classifies as presomitic mesoderm and somites, with some residual primitive streak. It expresses a number of mesodermal markers including *Mesp1*.
7,1	(endoderm)	7,0 exhibits strong classification for definitive endoderm and gut endoderm. It expresses definitive endodermal markers including *Foxa2* and *Sox17*. RNA velocity suggests 7,1 cells transition into 7,0, and largely classifies as anterior primitive streak and endoderm.
7,0		
7,2	Node	This cluster strongly classifies as node, and expresses *Chordin*.
0,4	(neuroectoderm) Early Ectoderm	This cluster classifies weakly as a number of ectodermal cell types, but based on RNA velocity seems to be most similar to early ectodermal cells.
0,2	(neuroectoderm) Early Ectoderm, Forebrain/ Midbrain fated	This cluster classifies weakly as a number of ectodermal cell types including early ectoderm. Based on RNA velocity, this cluster transitions into cluster 5 (forebrain/midbrain fated).
5	(neuroectoderm) Future Brain, Forebrain/ Midbrain	This cluster classifies strongly as forebrain/midbrain with some weaker future spinal cord classification. It expresses *Zic1* and *En2*.
9	(neuroectoderm) Future brain	This cluster classifies weakly as future brain, future spinal cord, and neural crest. It expresses *Crabp1* and *Tubb3*, and RNA velocity suggests it transitions from clusters 2 or 5.
0,3	Early Neuromesodermal Progenitor	This cluster classifies weakly as a number of cell types including primitive streak and early ectoderm, but more strongly as early neuromesodermal progenitor. RNA velocity shows cells in this cluster transition into a neuromesodermal progenitor. Cells in this cluster express *T* and some *Sox2*.
4	Neuromesodermal Progenitor	This cluster classifies strongly as neuromesodermal progenitor (late and early). It has some *T* and *Sox2* expression.
2	(neuroectoderm) Future Spinal Cord	This cluster classifies mostly as future spinal cord, and weakly as fore/midbrain. It also expresses many patterning genes from the Hox family indicative of spinal cord fated cells such as *Hoxb9*.

Table S2. Top regulators by PageRank in the mESC directed differentiation data, related to Note S3.
Top 10 regulators in each epoch network along each germ layer path are shown.

mesoderm		endoderm		neuroectoderm	
Gene	PageRank	Gene	PageRank	Gene	PageRank
epoch1		epoch1		epoch1	
Zfp42	0.150	Zfp42	0.105	Zfp42	0.087
Klf2	0.095	Klf2	0.072	Klf2	0.072
Sox2	0.049	Sox2	0.043	Utf1	0.070
Ncl	0.047	Ncl	0.039	Zfp990	0.039
Utf1	0.045	Utf1	0.037	Zfp985	0.026
Mtf2	0.022	Lyar	0.037	Ncl	0.024
Tcea3	0.011	Pa2g4	0.028	Lyar	0.024
Trp53	0.011	Mtf2	0.022	Rest	0.022
Jarid2	0.011	Trp53	0.018	Mtf2	0.019
Eno1	0.011	Tcea3	0.016	Pa2g4	0.018
epoch2		epoch2		epoch2	
Tead2	0.209	Tead2	0.103	Utf1	0.151
Sox11	0.072	Mis18bp1	0.084	Mis18bp1	0.048
Peg3	0.044	Cenpa	0.070	T	0.036
Cenpa	0.037	Ncl	0.039	Rest	0.030
Basp1	0.032	Lyar	0.036	Mtf2	0.028
Pcbp4	0.020	Pa2g4	0.026	Lyar	0.025
Cxxc5	0.019	Phf5a	0.020	Ncl	0.024
Sfpq	0.019	Sap30	0.019	Terf1	0.019
Jarid2	0.017	Jarid2	0.014	Pa2g4	0.017
Tcfl5	0.017	Sox11	0.013	Nanog	0.017
epoch3		epoch3		epoch3	
Tead2	0.134	Tead2	0.139	Vezf1	0.082
Sox11	0.042	Lhx1	0.047	Tead2	0.070
Bbx	0.039	Sox17	0.046	Sox11	0.041
Lhx1	0.027	Gata6	0.027	Hoxb9	0.029
Foxn3	0.026	Pitx2	0.024	Zmynd11	0.027
Basp1	0.020	Gsc	0.021	Hoxb2	0.026
Ndn	0.018	Ndn	0.017	Hoxa9	0.025
Gsc	0.017	Foxa1	0.017	Mllt3	0.024
Peg3	0.016	Foxa2	0.016	Hoxb8	0.022
Eomes	0.015	Basp1	0.015	Meis2	0.019

Table S3. Early functional differences in *in vitro* vs. *in vivo* networks, related to Figure 7 and S7. Enriched terms for *in vitro*-specific modules based on the Combined Score from Enrichr GSEA analysis, specific to the first epoch. These three communities belong to the first epoch and are activated in the *in vitro* data but not (or weakly activated) in the *in vivo* data (see **Fig S7**).

Term	Combined.Score
epoch 1, community 2	
positive regulation of stem cell proliferation (GO:2000648)	773.48
regulation of mRNA splicing, via spliceosome (GO:0048024)	203.75
epoch 1, community 3	
glutathione metabolic process (GO:0006749)	405.99
epoch 1, community 4	
cellular response to laminar fluid shear stress (GO:0071499)	1,027.54
myoblast fusion (GO:0007520)	859.88
response to laminar fluid shear stress (GO:0034616)	584.21
regulation of DNA methylation (GO:0044030)	584.21
cellular response to fluid shear stress (GO:0071498)	444.11
male gonad development (GO:0008584)	182.23
development of primary male sexual characteristics (GO:0046546)	182.23
regulation of protein metabolic process (GO:0051246)	155.19
gonad development (GO:0008406)	142.01

Note S1. Benchmarking Epoch against existing GRN reconstruction tools

To assess the performance of Epoch in reconstructing static networks, we benchmarked it on synthetically generated data. We generated fifteen synthetic datasets using the Dyngen R package (Cannoodt et al., 2021). Networks were designed to encompass varying regulatory motifs and spanned 100-420 genes including 20-70 transcription factors. Synthetic single-cell datasets generated from these networks varied in size, from as low as 20 to as high as 1000 cells. We compared Epoch to the original versions of GENIE3 (Huynh-Thu et al., 2010), which is the GRN reconstruction engine of SCENIC (Aibar et al., 2017), and CLR (Faith et al., 2007) as well as variations on these methods that incorporated them within the Epoch framework. Thus, we assessed a total of 11 methods: CLR using mutual information (original CLR), CLR using Pearson correlation, CLR using mutual information with cross-weighting, CLR using Pearson correlation with cross-weighting, GENIE3 (original GENIE3), GENIE3 limited to dynamically expressed genes, GENIE3 limited to dynamically expressed genes with cross-weighting, Epoch with Pearson correlation (with and without cross-weighting), and Epoch with mutual information (with and without cross-weighting).

We reconstructed individual networks with each method for each dataset, using normalized simulation time as the pseudotemporal annotation for Epoch. To assess performance, we compared each resulting network to a set of five random networks, unique to each reconstructed network, that were generated by permuting edge weights of targets for each transcription factor in the reconstructed network (**Fig S2A**). As a gold standard, all networks were compared against the original network used to generate the synthetic single-cell data. Based on fold improvement in area under the precision-recall curve over the random networks, all variations of Epoch outperformed original versions of CLR and GENIE3 (**Fig S2B**). Additionally, we found that Epoch using mutual information with or without cross-weighting resulted in higher fold improvement over random compared to any other method. The addition of cross-weighting improved median AUPR fold change over random for all methods. Further, limitation to dynamic genes (e.g. versions of CLR vs. corresponding versions of Epoch as well as GENIE3 vs. GENIE3 limited to dynamic genes) also improved performance. In all cases, it was apparent that key steps in the Epoch framework improved overall static reconstruction, as limiting reconstruction to dynamically expressed genes and applying the cross-weighting scheme both led to increased fold improvement in AUPR over random, demonstrating the utility of Epoch's framework.

We next compared Epoch to recently developed GRN reconstruction methods designed for single-cell data. We used the benchmarking platform, BEELINE (Pratapa et al., 2020), to assess Epoch's performance against 11 other single-cell methods across the synthetic datasets available within the tool (**Fig 2B, S3A**). Importantly, these covered a range of cell state trajectories (linear, long linear, bifurcating, bifurcating converging, cycle) as well as dataset sizes (100 to 5000 cells). Our results demonstrate that Epoch with cross-weighting (using either mutual information or Pearson correlation) performed best based on AUPR. Additionally, while SINCERITIES almost approaches Epoch's performance at the 5000-cell dataset size, it performs markedly worse with smaller datasets, unlike Epoch. Finally, additional comparison of computational runtimes demonstrated that Epoch has the additional benefit of running magnitudes more efficiently than other methods including GRNBOOST2, PIDC, and GENIE3 (**Fig S3B**).

We then compared Epoch against the same 11 single-cell GRN reconstruction methods across the curated datasets available in BEELINE (**Fig S3C**). Importantly these datasets, though synthetic, were simulated from literature-derived networks and pseudotime was computed using Slingshot (Street et al., 2018). In this case performance based on AUPR was more equal across the methods, with GENIE3, GRNBoost2, and PIDC slightly out-performing other methods (**Fig S3C i**). On closer inspection, it was clear that performance was dataset dependent. For example, Epoch and other pseudotime-based methods performed relatively better in reconstructing the GSD network vs the HSC network (**Fig S3C ii, iii**). The same phenomenon was present in the BEELINE publication where it was initially attributed to imprecision of trajectory inference in estimating pseudotime. To test this, we used the underlying literature derived-networks and re-simulated the datasets. We then used the true simulation time, rather than Slingshot-derived pseudotime, for reconstruction and benchmarking. Our results demonstrated that despite using the true simulation time, AUPR of pseudotime-based reconstruction methods was largely unchanged, suggesting that poor pseudotime computation was not at fault (**Fig S3C iv**).

Finally, we hypothesized that decreased performance in the pseudotime-based methods was largely driven by reconstruction on split trajectories. Namely, for pseudotime-based methods, reconstruction of branched data was performed along each lineage separately and resulting networks

were aggregated. For example, HSC datasets represented four distinct lineages (branches), and so the 2000 cell dataset was broken into roughly four 500 cell datasets for reconstruction by pseudotime-based methods before aggregation. For non-pseudotime-based methods, including GENIE3, GRNBoost2, and PIDC, reconstruction was done on the full 2000 cell dataset. To test the extent to which this impacted performance, we re-benchmarked GENIE3, GRNBoost2, and PIDC splitting the reconstruction along each lineage before aggregating, mirroring the pseudotime-based methods. The resulting performance was substantially decreased, suggesting that splitting reconstruction is a factor contributing to decreased performance (**Fig S3D**). Ultimately, other factors, such as network density and the presence of specific connectivity motifs, warrant further exploration, but was unfortunately infeasible with the limited data.

Next, while the results from assessment of networks reconstructed from synthetic data demonstrated Epoch's favorable performance as a network inference tool, we acknowledge that there are caveats associated with synthetic data, including limited stochasticity and reliance on simulations that may not encompass the full extent of potential cell state responses seen in real biological systems. Thus, we next turned our attention to benchmarking on real world data. To assess Epoch's performance, we began by assessing the networks reconstructed by the variations of Epoch, CLR and GENIE3 listed above from data of E12.5 mouse muscle development (**Fig S2C-E**). For this dataset, we used Diffusion based pseudotime (DPT) to compute pseudotime for Epoch reconstruction (Haghverdi et al., 2016). We used Chip-X data from the Enrichr database, which includes ChIP-Seq, ChIP-ChIP, ChIP-PET, DamID used to profile transcription factor binding to DNA, covering 220 TFs and >35,000 genes, as a gold standard network (Lachmann et al., 2010). Based on precision recall, we found that all variations of Epoch once again outperformed original versions of CLR and GENIE3. Interestingly, we found that the two variations of GENIE3 embedded within the Epoch framework performed best overall in this assessment, followed by the two variations of Epoch using mutual information (with and without cross-weighting). It was again apparent that limiting reconstruction to dynamically expressed genes and cross-weighting significantly improved overall reconstruction (**Fig S2E**).

To determine if these results were consistent across other real world datasets, we turned to single-cell transcriptomic data collected from day 4 *in vitro* mESC directed differentiation (Spangler et al., 2018). We limited our reconstruction to cells in earlier stages of differentiation that had not yet transitioned into any committed germ layer-like state, as determined by pseudotemporal analysis, RNA velocity analysis, expression of *Zfp42*, marking naive pluripotent cells, and expression of *Fgf5*, marking cells in a primed state (**Fig S2F**). The filtering ensured the trajectory remained linear, which, while absolutely not a requirement for Epoch reconstruction, was employed to minimize performance variability of trajectory inference methods in which branched structures may be more difficult to order. This allowed us to narrow our focus on reconstruction performance while minimizing impact from potentially inaccurate pseudotemporal ordering. Based on precision-recall, we found that Epoch variations using cross-weighting performed best, followed by GENIE3 embedded within the Epoch framework (**Fig S2G**). Overall, these benchmarking results demonstrate Epoch's utility as a reconstruction tool, and further demonstrate the usefulness of Epoch as a flexible framework that can improve reconstruction of other methods.

Note S2. Early *in vitro* mouse ESC directed differentiation cluster annotations

We annotated the *in vitro* mESC directed differentiation clusters based on gene marker expression, differential expression analysis, RNA velocity analysis, and singleCellNet classification (**Fig 3B-D, S4**). Undifferentiated cells populated cluster 1, which was positive for *Zfp42* expression, a pluripotency marker (Rogers et al., 1991). This population additionally classified as inner cell mass, further supporting their pluripotent annotation. RNA velocity indicated these cells transitioned into cluster 3, which marked the beginning of *Fgf5* expression, an epiblast maker (Haub and Goldfarb, 1991; Pelton et al., 2002). SCN revealed early ectoderm and epiblast signature for cluster 3, indicating to us that it was representative of a primed cell state. Cells in this cluster transitioned to cluster 0 and 0,4. Cells in cluster 0 were largely representative of primitive streak, as determined by *Brachyury* expression, with some early ectoderm and residual epiblast signature, as determined by SCN. Interestingly, cluster 0,4, which expressed a lower level of *Brachyury* and exhibited some primitive streak and early ectoderm SCN signature, was comprised of day 0 cells. It is possible that these cells, which had yet to undergo the

differentiation protocol, had escaped LIF-controlled naïve pluripotency and were already in a primed early ectodermal state.

Cluster 0 cells expressing *Mixl1*, a regulator of mesoderm and endoderm (Hart et al., 2002) further branched into two distinct lineages according to RNA velocity: mesoderm (cluster 8) and endoderm (clusters 7,1 and 7,0). Cluster 8 was largely enriched for *Mesp1*, and some cells at later time (determined by RNA velocity) in this cluster also expressed *Tbx6*. SCN analysis revealed that this cluster exhibited multiple mesoderm-related signatures including primitive streak, anterior paraxial mesoderm, presomitic mesoderm, and somites, ultimately supporting its mesoderm annotation. Along the endoderm path, cluster 7,1 transitioned from cluster 0 and further transitioned into cluster 7,0. Both 7,1 and 7,0 are enriched for *Foxa2* and *Sox17* expression. SCN analysis suggested an increasing endodermal signature down this path, with cluster 7,1 classifying as anterior primitive streak and weaker as definitive endoderm and gut endoderm, while cluster 7,0 more strongly classified as definitive and gut endoderm.

The neuroectodermal path begins from both cluster 0 and 0,4 according to RNA velocity results. We annotated clusters 0,3 and 4 as neuromesodermal progenitor (NMP) populations. SCN further verified cluster 0,3, which expresses *T* and *Sox2*, as early NMP and cluster 4, which expresses *Sox2* and exhibits variable *T* expression, as late NMP. Cluster 7,2, which expresses *Chordin*, classified strongly as node. Interestingly, RNA velocity suggested the existence of two parallel paths along the neuroectodermal lineage, with cluster 0,2 transitioning into cluster 5, and cluster 4 transitioning into cluster 2. Along the first path, cluster 0,2, classified weakly as a number of ectodermal cell types including early ectoderm. Because RNA velocity indicated this cluster transitioned into the later neuroectoderm cluster 5, we annotated it as early ectoderm. Cluster 5 classified strongly as forebrain/midbrain, with some weaker future spinal cord classification. Given this, and it's *Zic1* and *En2* expression, we annotated this cluster as future brain. Cluster 9, which expresses *Crabp1* and differentially expresses *Tubb3* (suggesting a later neuronal identity compared to cluster 2 or 5), seems to transition from this cluster, and is thus annotated as future brain. Along the second neuroectodermal path, cells in cluster 2 classified more strongly as future spinal cord with a weaker forebrain/midbrain classification. Importantly this cluster expresses many patterning genes from the Hox family indicative of spinal cord fated cells, including *Hoxd9* and *Hoxb6* (Philippidou and Dasen, 2013). For this reason, we annotated this cluster as future spinal cord. A summary of our cluster labels can be found in the supplemental tables (**Table S1**).

Note S3. Epoch elucidates regulatory networks driving lineage specification in early *in vitro* mouse ESC differentiation

To begin our network analysis exploring lineage specification, we applied Epoch to the day 0 through day 4 directed differentiation data, using latent time (Bergen et al., 2020) to order cells, and reconstructing the networks underlying each of the three lineages. Latent time was divided into three epochs, and a dynamic network was extracted for each lineage (**Fig S5A-C**). In examining the Epoch-predicted top regulators and their top targets (**Fig S5D, Table S2**), we observed noteworthy regulatory programs emerging over time along the three lineages. For example, a module including the genes *Gsc*, *Lhx1*, *Sox17*, *Foxa1*, *Foxa2*, and *Gata6* emerges in the third epoch along the endoderm path. *Sox17* and *Foxa2* serve as endoderm markers, as knockout of *Sox17* has been shown to deplete definitive gut endoderm and lack of *Foxa2* results in failure to develop fore- and midgut endoderm (Dufort et al., 1998; Kanai-Azuma et al., 2002). *Foxa1* has also been implicated in the initiation and maintenance of the endodermal lineage (Ang et al., 1993), while inactivation of *Lhx1*, which has been shown to bind to the enhancer region of *Foxa2*, disrupts the development of definitive endoderm (Costello et al., 2015). The regulator *Sox11* and a collection of Hox genes emerge in the third epoch of the neuroectoderm lineage, suggesting the activation of programs that pattern brain and spinal cord (Philippidou and Dasen, 2013). Ultimately, these networks served as a foundation for the remainder of the analyses in this study, representing TF-target regulation present along each path of lineage specification.

In addition to directly extracting top regulators via PageRank and Betweenness-Degree from the reconstructed lineage networks, we highlight a more nuanced methodology to resolve influential TFs based on bagging, since the consensus of many reconstructed networks would be less susceptible to noise. Specifically, we limited our scope to early time, corresponding to a naïve to primed pluripotency transition, and bootstrapped the network reconstruction (**Fig S5E-G**). For each of these sampled and reconstructed networks, we predicted the top 10 regulators involved in the transition by both PageRank

and Betweenness-Degree. We then applied a consensus approach in which regulators were ranked by their frequency as a top 10 regulator (based on PageRank) or average importance (based on Betweenness-Degree) amongst the bootstrapped networks. The top regulators recovered by both PageRank and Betweenness-Degree were largely overlapping, and included TFs such as *Zfp42*, *Klf2*, *Sox11*, *Pou3f1*, and *Klf4*.

Of the top 10 regulators predicted through this consensus approach, *Klf2* and *Klf4* are critical in maintaining ground state pluripotency (Yeo et al., 2014). For example, it has been demonstrated that nuclear export of *Klf4* causes rapid decline in *Klf4* transcription, a trigger that leads to the exit of naïve pluripotency, and the blocking of which prevents ESC differentiation (Dhaliwal et al., 2018). Thus, it is unsurprising that they are predicted to have an influential role in dictating network topology. Interestingly, a number of predicted top regulators, such as *Pou3f1* and *Sox11*, are known to promote neural fate (Barral et al., 2019; Wang et al., 2013; Zhu et al., 2014). Knockdown of another predicted top regulator, *Tcea3*, has also been shown to bias differentiation toward mesendodermal fates (Park et al., 2013). Taken together, this suggests that the underlying network is primed for the neuroectodermal specification fate choice, aligning with the default model of neural induction in mESCs (Muñoz-Sanjuán and Brivanlou, 2002; Tropepe et al., 2001) and the apparent preference for neuroectoderm fate amongst cells in this dataset.

Note S4. *In vivo* dynamic network top regulator prediction

Of the 22 unique top regulators in the second and third epochs of the *in vivo* mesoderm network (**Fig 7A**), at least 17 have known roles in guiding exit from pluripotency, mesoderm specification, or somitogenesis. In particular, a number of top regulators in the second epoch are required for guiding the exit of pluripotency, such as *Nr6a1* and *Snai1* (Galvagni et al., 2015; Gu et al., 2005). Others in this epoch are components of the Wnt signaling pathway including *Lef1*, a Wnt effector, and *Sp5*, which itself is directly activated by Wnt signals and further aids in activating Wnt target genes to promote differentiation into multipotent mesodermal progenitors (Kennedy et al., 2016). Further, TFs like *Brachyury* and *Lhx1* are necessary for primitive streak formation and normal development of primitive streak-derived tissues (Shawlot et al., 1999; Wilson et al., 1995). Spread across both the second and third epochs are a number TFs responsible for patterning and promoting mesoderm fate. These include TFs like *Hoxb1*, *Hoxb2*, *Hoxb9*, *Cdx1*, *Cdx2*, *Mesp1*, *Meis2*, and *Id1* (Bernardo et al., 2011; Cecconi et al., 1997; Foley et al., 2019; Gouveia et al., 2015; Malaguti et al., 2013; Roux et al., 2015; Takahashi et al., 2005, 2007). Of these, many are also responsible for inhibiting alternative fates, such as *Id1*'s role in inhibiting neural induction and *Cdx2*'s role in blocking cardiac differentiation (Mendjan et al., 2014; Zhang et al., 2010). Finally, at least two TFs in the third epoch, *Tbx6* and *Hes7*, are essential for specifying and coordinating somitogenesis (Bessho et al., 2001; Chapman et al., 2003). Ultimately, the predicted top regulators match well with prior literature describing the ESC to presomitic mesoderm lineage trajectory from which the network was reconstructed. Additionally, this further corroborates Epoch's usefulness and ability in isolating important genes driving dynamic processes.

Supplemental Experimental Procedures

mESC maintenance and differentiation

GFP-Brychyury mESC cells (Gadue et al., 2006) were maintained and differentiated through day 2 of the directed differentiation protocol according to Spangler et al. (Spangler et al., 2018). At day 2, four different primitive-streak induction treatments were established by adding growth factors Wnt3a (25ng/mL) and Activin A (WA; 9ng/mL) along with one of the following additional growth factors: Noggin (150ng/mL), Gsk inhibitor (10mM), or BMP4 (0.5ng/mL). On the day of sequencing, EBs and monolayers were dissociated to a single-cell suspension through the use of TrypLE and 40uM cell strainers.

Multi-Seq protocol

We utilized the MULTI-seq sample barcoding and library preparation protocol (McGinnis et al., 2019) in order to sequence all samples in one 10x capture run. In short, the protocol involved tagging cell membranes with sample specific barcodes using a lipid-modified oligonucleotide (LMO). The LMOs (reagents obtained from the McGinnis lab) anchor into the cell membrane and allow for the attachment of a normal ssDNA oligonucleotide (MULTI-Seq barcode). A unique MULTI-seq barcode was added to each sample after which, all samples were pooled and sequenced as if they were one sample. An equal number of cells from each sample were combined to make up the pooled samples and ensure equal representation of each sample after down-stream sequencing. MULTI-Seq barcodes were used down-stream to identify which cells were from which samples.

Library preparation and sequencing

After cells were successfully tagged and pooled, they were submitted to a sequencing core facility for 10x capture and library preparation. A Truseq library preparation was performed with the necessary adjustments made to accommodate the MULTI-Seq platform. Libraries were sequenced on Illumina NovaSeq.

Single-cell data processing

Sequencing alignment to the mm10 reference genome was performed using CellRanger (version 3.1), and spliced, unspliced, and ambiguous read counts were extracted using Velocyto. Sample barcode classification was performed using the deMULTIplex R package (https://github.com/chris-mcginnis-ucsf/MULTI-seq). Subsequent quality control filtering, normalization, clustering, and differential gene expression analysis was performed using Scanpy (version 1.4.5) (Wolf et al., 2018). Specifically, doublets and negatives from the sample barcode classification were removed, along with 271 cells we identified as residual fibroblasts (Thy1+). Next, genes were excluded if they were detected in less than 5 cells; cells were excluded if their mitochondrial gene content exceeded 10% of their total reads or if they had fewer than 500 unique genes. This left us with 5530 cells and 17528 genes. The data was then normalized and log transformed before highly variable genes were identified (1938 genes). The data was scaled and PCA was performed. Leiden clustering was performed and visualized on a UMAP embedding. We further removed a cluster of possible dying cells expressing relatively high mitochondrial gene content and low total read count, leaving a dataset with 5228 cells and 1938 variable genes. Leiden clustering was refined, and RNA velocity was computed using scvelo (version 0.2.2) (Bergen et al., 2020). Latent time was computed with scvelo, using root and end states that were computed through CellRank (version 1.0.0-rc.0). Cell type classification was performed via SingleCellNet (Tan and Cahan, 2019), using complied embryo data for training the classifier. For the E12.5 muscle development data and day 4 early directed differentiation data, diffusion maps and diffusion pseudotime were computed through Scanpy.

CLR

The Context Likelihood of Relatedness (CLR) algorithm was first proposed in 2007 by Faith et al. as a method for inferring gene regulatory networks from expression data. In short, CLR computes the mutual

information (MI) between expression levels of every potential transcription factor and target gene. From here the method scores the MI values in the context of the network by computing a z-score relying on (1) the distribution of MI values for all potential regulators of the target gene, z_i, and on (2) the distribution of MI values for all potential targets of the transcription factor, z_j:

$$z_{ij} = \sqrt{z_i^2 + z_j^2}$$

The result is a weighted adjacency matrix describing the likelihood of TF-target gene interactions that can be thresholded to derive a network structure. For Epoch, a version of CLR is applied to dynamically expressed genes to reconstruct an initial static network via the 'minet' package in R. Users can choose between implementing the MI version or a version using Pearson correlation in place of MI. In either case, Epoch at this step will return a GRN table. Each row outlines an interaction in the initial network identifying the transcription factor, target gene, correlation, and CLR-based z-score.

Synthetic benchmarking

15 synthetic datasets were generated using the Dyngen package in R (Cannoodt et al., 2021). Specifically, networks were generated with 100-420 genes (including 20-70 TFs), containing varied topological motifs, and cell trajectories were simulated over time. Simulated single-cell sequencing was performed, resulting in datasets that included up to 1000 cells. CLR was implemented with the minet package in R (Meyer et al., 2008), and GENIE3 was implemented with the GENIE3 package in R (Aibar et al., 2017; Huynh-Thu et al., 2010). Variations of these two methods were carried out using the Epoch framework. Performance (AUPR) was compared against sets of 5 random networks generated for each reconstructed network via the random permutation of edge weights across targets.

BEELINE benchmarking

The BEELINE benchmarking tool (Pratapa et al., 2020) was used to compare Epoch against the following single-cell reconstruction methods (using the pre-built Docker images from BEELINE): GENIE3, GRISLI, GRNBoost2, GRNVBEM, LEAP, PIDC, PPCOR, SCODE, SCRIBE, SINCERITIES, and SINGE. We added the four versions of Epoch into the BEELINE framework for benchmarking. The synthetic and curated datasets (including simulation time and pseudotime) on which we did the benchmarking were the same as those used in the BEELINE publication, and downloaded from https://doi.org/10.5281/zenodo.3378975. Briefly, for synthetic datasets, each trajectory type included 5 dataset sizes (100 cells, 200 cells, 500 cells, 2000 cells, and 5000 cells), and each dataset size included 10 distinct datasets (for a total of 50 datasets for each trajectory type). Curated datasets were simulated from four literature derived networks (GSD: gonadal sex determination, HSC: hematopoietic stem cell differentiation, VSC: ventral spinal cord, mCAD: mammalian cortical area development). 10 datasets were simulated for each network at 3 different dropout levels (0%, 50%, 70%), for a total of 30 datasets per network. AUPR, early precision, and runtimes were evaluated. BoolODE (Pratapa et al., 2020) was used to re-simulate the curated datasets for the purposes of extracting the true simulation time.

Bootstrapped network reconstruction of early MULTI-seq data

We isolated early latent time clusters 1 and 3 and uniformly sampled 400 cells, 10 times to reconstruct 10 networks. For each reconstructed network, we extracted top regulators by PageRank and identified TFs that were most frequently ranked in the top 10 regulators. We further computed the average normalized betweenness and average normalized degree across the 10 reconstructed networks to identify top regulators.

Differential network analysis and assessment

As one method of network comparison, we used a naïve edge weight-based approach to extract the most differentially weighted edges between networks. Briefly, this involves computing edge weight differences for each possible edge in the two networks. Edges are then considered "differential" and specific to a given network if the edge weight difference is greater than a given threshold (in the case of both the treatment difference analysis and the *in vivo* vs. *in vitro* comparison, this threshold was set to 2). Such an

approach resulted in “differential networks” which are representative of unique topological features existing in each treatment-specific network. To assess the feasibility of this simple method in extracting real and important topological differences between networks, we first applied the same method to compare the three lineage networks in the dataset. The ground truth on which we assessed these differential networks was a set of lineage-unique “pseudo-ChIP-seq” networks we compiled similar to TF-promoter binding predictions generated by (Lu and Mar, 2020). In short, TF-target interactions were acquired by mapping the PWM of a TF (Weirauch et al., 2014) to the promoter region sequence of potential target genes using the Find Individual Motif Occurrences (FIMO) software (described in more detail below). These ground truth networks were filtered for dynamically expressed genes along given paths (for lineage-specificity), and further filtered for unique edges to mimic extraction of unique topological features (lineage-unique). Using this set of networks, we compared AUPR of our path-differential networks against random networks (generated by shuffling edge weights of targets of each TF in the differential networks). On average the differential networks had a 1.7 fold improvement over random AUPR, with many comparisons falling in the 1.8-3.0 range (data not shown).

Construction of path-unique TF-target pseudo-gold standard

Transcription star site (TSS) annotations were downloaded from the USCS Genome Browser (mouse GRCm38/mm10 genome assembly) (Haeussler et al., 2019). Promoter regions were defined as -750 to +250 around the TSSs. We then acquired position weight matrices (PWMs) of transcription factors from the Catalog of Inferred Sequence Binding Preferences (CIS-BP Database build version 2.00) (Weirauch et al., 2014). We used the Find Individual Motif Occurrences tool (Grant et al., 2011) to obtain potential TF-promoter binding pairs for 648 TFs. We kept all interactions for which p-value < 5×10^{-5}. To generate path-unique gold standards, for each lineage (mesoderm, endoderm, neuroectoderm) we filtered interactions for dynamically expressed genes along each path as computed by Epoch. Further, when assessing the “differential network” pairwise comparisons, we filtered out interactions that were redundant between the gold standards, and only kept interactions unique to each path.

Comprehensive signaling effector TF targets list

We acquired binding score (MACS2) data for 18 signaling effector TFs from the ChIP-Atlas (Oki et al., 2018), and processed each accordingly: target genes were ranked by maximum binding score and the top 2000 targets were retained (or all retained, if less than 2000 targets). To compute average effector activity, target lists were filtered for those appearing in the MULTI-seq directed differentiation data, and not considered in the analysis if the effector had less than 10 targets after filtering.

Targets of TFs by treatment comparison

To quantify the extent of topology differences between treatments along the mesodermal path, we performed pairwise comparison on the four treatment-specific networks and computed Jaccard similarity between predicted targets of TFs. The comparison was carried out on 72 TFs that were selected based on their active expression on day 3 or day 4 (i.e. after induction treatments). We computed baseline similarities for each TF in each treatment by bootstrapping the network reconstruction (10 network reconstructions per treatment, 400 sampled cells per network reconstruction) and averaging their pairwise Jaccard similarities. We selected the 13 TFs exhibiting the greatest differences in targets amongst the treatments and performed gene set enrichment analysis using the Enrichr R package (Chen et al., 2013; Kuleshov et al., 2016) and the GO Consortium Biological Processes database (Ashburner et al., 2000; Gene Ontology Consortium, 2021) on the targets of each TF. We further filtered out terms that did not meet the criteria of adjusted p-value<0.05. Finally, we summarized the results between the 13 TFs by counting the frequency (out of 13) that a term was considered enriched and ranked the results accordingly.

In vivo comparison

To create a comparable in vivo dataset, 250 cells were randomly sampled from each of the following annotated populations in the Grosswendt et al. gastrulation dataset: “Primitive streak anterior”,

“Endoderm”, “Ectoderm early 1”, “Ectoderm early 2”, “Epiblast”, “Fore_midbrain”, “Future spinal cord”, “Endoderm gut”, “Neural crest”, “Ectoderm neural anterior”, “Ectoderm neural posterior”, “Neuromesodermal progenitor late”, “Node”, “Notochord”, “Mesoderm pharyngeal arch”, “Mesoderm presomitic”, “Primitive streak late”, “Primitive streak early”, “Somites”, “Neuromesodermal progenitor early.” The resulting dataset spanned E6.5 to E8.5. Quality control filtering, normalization, and Diffusion Pseudotime trajectory inference was performed using Scanpy (version 1.4.5) (Wolf et al., 2018), analogous to the processing of the MULTI-Seq data described above. Further comparison was limited to the mesodermal lineage – this included populations labeled “Epiblast”, “Primitive streak early”, “Primitive streak late”, and “Mesoderm presomitic”.

Epoch was employed to reconstruct the in vivo dynamic network corresponding to this data. To compare the *in vivo* network to the *in vitro* network, both networks were thresholded such that the top 2% of non-zero edges were kept. Network comparison including differential network extraction and community detection were performed using Epoch. Average module expression was analyzed by computing mean expression of predicted activated members over time if the module included at least 8 such members (members predicted to be repressed were not included in the average so as not to improperly depress this measure of activity). GSEA was performed using the Enrichr R package (Chen et al., 2013; Kuleshov et al., 2016) and the GO Consortium Biological Processes database (Ashburner et al., 2000; Gene Ontology Consortium, 2021). Both the 2021 and 2018 versions of this database were used for enrichment analyses. Figures shown here show results using the 2021 version of this database for all enrichment analyses except for epoch3, community 3. This community was not enriched for any terms in the 2021 database, but was enriched for multiple terms in the 2018 pathway.

Supplemental References

Aibar, S., González-Blas, C.B., Moerman, T., Huynh-Thu, V.A., Imrichova, H., Hulselmans, G., Rambow, F., Marine, J.-C., Geurts, P., Aerts, J., et al. (2017). SCENIC: single-cell regulatory network inference and clustering. Nat. Methods *14*, 1083–1086.

Ang, S.L., Wierda, A., Wong, D., Stevens, K.A., Cascio, S., Rossant, J., and Zaret, K.S. (1993). The formation and maintenance of the definitive endoderm lineage in the mouse: involvement of HNF3/forkhead proteins. Development *119*, 1301–1315.

Ashburner, M., Ball, C.A., Blake, J.A., Botstein, D., Butler, H., Cherry, J.M., Davis, A.P., Dolinski, K., Dwight, S.S., Eppig, J.T., et al. (2000). Gene Ontology: tool for the unification of biology. Nat. Genet. *25*, 25–29.

Barral, A., Rollan, I., Sanchez-Iranzo, H., Jawaid, W., Badia-Careaga, C., Menchero, S., Gomez, M.J., Torroja, C., Sanchez-Cabo, F., Göttgens, B., et al. (2019). Nanog regulates Pou3f1 expression at the exit from pluripotency during gastrulation. Biol. Open *8*.

Bergen, V., Lange, M., Peidli, S., Wolf, F.A., and Theis, F.J. (2020). Generalizing RNA velocity to transient cell states through dynamical modeling. Nat. Biotechnol. *38*, 1408–1414.

Bernardo, A.S., Faial, T., Gardner, L., Niakan, K.K., Ortmann, D., Senner, C.E., Callery, E.M., Trotter, M.W., Hemberger, M., Smith, J.C., et al. (2011). BRACHYURY and CDX2 mediate BMP-induced differentiation of human and mouse pluripotent stem cells into embryonic and extraembryonic lineages. Cell Stem Cell *9*, 144–155.

Bessho, Y., Sakata, R., Komatsu, S., Shiota, K., Yamada, S., and Kageyama, R. (2001). Dynamic expression and essential functions of Hes7 in somite segmentation. Genes Dev. *15*, 2642–2647.

Cannoodt, R., Saelens, W., Deconinck, L., and Saeys, Y. (2021). Spearheading future omics analyses using dyngen, a multi-modal simulator of single cells. Nat. Commun. *12*, 3942.

Cecconi, F., Proetzel, G., Alvarez-Bolado, G., Jay, D., and Gruss, P. (1997). Expression of Meis2, a Knotted-related murine homeobox gene, indicates a role in the differentiation of the forebrain and the somitic mesoderm. Dev. Dyn. *210*, 184–190.

Chapman, D.L., Cooper-Morgan, A., Harrelson, Z., and Papaioannou, V.E. (2003). Critical role for Tbx6 in mesoderm specification in the mouse embryo. Mech. Dev. *120*, 837–847.

Chen, E.Y., Tan, C.M., Kou, Y., Duan, Q., Wang, Z., Meirelles, G.V., Clark, N.R., and Ma'ayan, A. (2013). Enrichr: interactive and collaborative HTML5 gene list enrichment analysis tool. BMC Bioinformatics *14*, 128.

Costello, I., Nowotschin, S., Sun, X., Mould, A.W., Hadjantonakis, A.-K., Bikoff, E.K., and Robertson, E.J. (2015). Lhx1 functions together with Otx2, Foxa2, and Ldb1 to govern anterior mesendoderm, node, and midline development. Genes Dev. *29*, 2108–2122.

Dhaliwal, N.K., Miri, K., Davidson, S., Tamim El Jarkass, H., and Mitchell, J.A. (2018). KLF4 Nuclear Export Requires ERK Activation and Initiates Exit from Naive Pluripotency. Stem Cell Rep. *10*, 1308–1323.

Dufort, D., Schwartz, L., Harpal, K., and Rossant, J. (1998). The transcription factor HNF3beta is required in visceral endoderm for normal primitive streak morphogenesis. Development *125*, 3015–3025.

Faith, J.J., Hayete, B., Thaden, J.T., Mogno, I., Wierzbowski, J., Cottarel, G., Kasif, S., Collins, J.J., and Gardner, T.S. (2007). Large-scale mapping and validation of Escherichia coli transcriptional regulation from a compendium of expression profiles. PLoS Biol. *5*, e8.

Foley, T.E., Hess, B., Savory, J.G.A., Ringuette, R., and Lohnes, D. (2019). Role of Cdx factors in early mesodermal fate decisions. Development *146*.

Gadue, P., Huber, T.L., Paddison, P.J., and Keller, G.M. (2006). Wnt and TGF-beta signaling are required for the induction of an in vitro model of primitive streak formation using embryonic stem cells. Proc. Natl. Acad. Sci. USA *103*, 16806–16811.

Galvagni, F., Lentucci, C., Neri, F., Dettori, D., De Clemente, C., Orlandini, M., Anselmi, F., Rapelli, S., Grillo, M., Borghi, S., et al. (2015). Snai1 promotes ESC exit from the pluripotency by direct repression of self-renewal genes. Stem Cells *33*, 742–750.

Gene Ontology Consortium (2021). The Gene Ontology resource: enriching a GOld mine. Nucleic Acids Res. *49*, D325–D334.

Gouveia, A., Marcelino, H.M., Gonçalves, L., Palmeirim, I., and Andrade, R.P. (2015). Patterning in time and space: HoxB cluster gene expression in the developing chick embryo. Cell Cycle *14*, 135–145.

Grant, C.E., Bailey, T.L., and Noble, W.S. (2011). FIMO: scanning for occurrences of a given motif.

Bioinformatics *27*, 1017–1018.
Gu, P., LeMenuet, D., Chung, A.C.-K., Mancini, M., Wheeler, D.A., and Cooney, A.J. (2005). Orphan nuclear receptor GCNF is required for the repression of pluripotency genes during retinoic acid-induced embryonic stem cell differentiation. Mol. Cell. Biol. *25*, 8507–8519.
Haeussler, M., Zweig, A.S., Tyner, C., Speir, M.L., Rosenbloom, K.R., Raney, B.J., Lee, C.M., Lee, B.T., Hinrichs, A.S., Gonzalez, J.N., et al. (2019). The UCSC Genome Browser database: 2019 update. Nucleic Acids Res. *47*, D853–D858.
Haghverdi, L., Büttner, M., Wolf, F.A., Buettner, F., and Theis, F.J. (2016). Diffusion pseudotime robustly reconstructs lineage branching. Nat. Methods *13*, 845–848.
Hart, A.H., Hartley, L., Sourris, K., Stadler, E.S., Li, R., Stanley, E.G., Tam, P.P.L., Elefanty, A.G., and Robb, L. (2002). *Mixl1* is required for axial mesendoderm morphogenesis and patterning in the murine embryo. Development *129*, 3597–3608.
Haub, O., and Goldfarb, M. (1991). Expression of the fibroblast growth factor-5 gene in the mouse embryo. Development *112*, 397–406.
Huynh-Thu, V.A., Irrthum, A., Wehenkel, L., and Geurts, P. (2010). Inferring regulatory networks from expression data using tree-based methods. PLoS One *5*.
Kanai-Azuma, M., Kanai, Y., Gad, J.M., Tajima, Y., Taya, C., Kurohmaru, M., Sanai, Y., Yonekawa, H., Yazaki, K., Tam, P.P.L., et al. (2002). Depletion of definitive gut endoderm in Sox17-null mutant mice. Development *129*, 2367–2379.
Kennedy, M.W., Chalamalasetty, R.B., Thomas, S., Garriock, R.J., Jailwala, P., and Yamaguchi, T.P. (2016). Sp5 and Sp8 recruit β-catenin and Tcf1-Lef1 to select enhancers to activate Wnt target gene transcription. Proc. Natl. Acad. Sci. USA *113*, 3545–3550.
Kuleshov, M.V., Jones, M.R., Rouillard, A.D., Fernandez, N.F., Duan, Q., Wang, Z., Koplev, S., Jenkins, S.L., Jagodnik, K.M., Lachmann, A., et al. (2016). Enrichr: a comprehensive gene set enrichment analysis web server 2016 update. Nucleic Acids Res. *44*, W90-7.
Lachmann, A., Xu, H., Krishnan, J., Berger, S.I., Mazloom, A.R., and Ma'ayan, A. (2010). ChEA: transcription factor regulation inferred from integrating genome-wide ChIP-X experiments. Bioinformatics *26*, 2438–2444.
Lu, T., and Mar, J.C. (2020). Investigating transcriptome-wide sex dimorphism by multi-level analysis of single-cell RNA sequencing data in ten mouse cell types. Biol. Sex Differ. *11*, 61.
Malaguti, M., Nistor, P.A., Blin, G., Pegg, A., Zhou, X., and Lowell, S. (2013). Bone morphogenic protein signalling suppresses differentiation of pluripotent cells by maintaining expression of E-Cadherin. Elife *2*, e01197.
McGinnis, C.S., Patterson, D.M., Winkler, J., Conrad, D.N., Hein, M.Y., Srivastava, V., Hu, J.L., Murrow, L.M., Weissman, J.S., Werb, Z., et al. (2019). MULTI-seq: sample multiplexing for single-cell RNA sequencing using lipid-tagged indices. Nat. Methods *16*, 619–626.
Mendjan, S., Mascetti, V.L., Ortmann, D., Ortiz, M., Karjosukarso, D.W., Ng, Y., Moreau, T., and Pedersen, R.A. (2014). NANOG and CDX2 pattern distinct subtypes of human mesoderm during exit from pluripotency. Cell Stem Cell *15*, 310–325.
Meyer, P.E., Lafitte, F., and Bontempi, G. (2008). minet: A R/Bioconductor package for inferring large transcriptional networks using mutual information. BMC Bioinformatics *9*, 461.
Muñoz-Sanjuán, I., and Brivanlou, A.H. (2002). Neural induction, the default model and embryonic stem cells. Nat. Rev. Neurosci. *3*, 271–280.
Oki, S., Ohta, T., Shioi, G., Hatanaka, H., Ogasawara, O., Okuda, Y., Kawaji, H., Nakaki, R., Sese, J., and Meno, C. (2018). ChIP-Atlas: a data-mining suite powered by full integration of public ChIP-seq data. EMBO Rep. *19*.
Park, K.-S., Cha, Y., Kim, C.-H., Ahn, H.-J., Kim, D., Ko, S., Kim, K.-H., Chang, M.-Y., Ko, J.-H., Noh, Y.-S., et al. (2013). Transcription elongation factor Tcea3 regulates the pluripotent differentiation potential of mouse embryonic stem cells via the Lefty1-Nodal-Smad2 pathway. Stem Cells *31*, 282–292.
Pelton, T.A., Sharma, S., Schulz, T.C., Rathjen, J., and Rathjen, P.D. (2002). Transient pluripotent cell populations during primitive ectoderm formation: correlation of in vivo and in vitro pluripotent cell development. J. Cell Sci. *115*, 329–339.
Philippidou, P., and Dasen, J.S. (2013). Hox genes: choreographers in neural development, architects of circuit organization. Neuron *80*, 12–34.
Pratapa, A., Jalihal, A.P., Law, J.N., Bharadwaj, A., and Murali, T.M. (2020). Benchmarking algorithms for gene regulatory network inference from single-cell transcriptomic data. Nat. Methods *17*, 147–154.

Rogers, M.B., Hosler, B.A., and Gudas, L.J. (1991). Specific expression of a retinoic acid-regulated, zinc-finger gene, Rex-1, in preimplantation embryos, trophoblast and spermatocytes. Development *113*, 815–824.
Roux, M., Laforest, B., Capecchi, M., Bertrand, N., and Zaffran, S. (2015). Hoxb1 regulates proliferation and differentiation of second heart field progenitors in pharyngeal mesoderm and genetically interacts with Hoxa1 during cardiac outflow tract development. Dev. Biol. *406*, 247–258.
Shawlot, W., Wakamiya, M., Kwan, K.M., Kania, A., Jessell, T.M., and Behringer, R.R. (1999). Lim1 is required in both primitive streak-derived tissues and visceral endoderm for head formation in the mouse. Development *126*, 4925–4932.
Spangler, A., Su, E.Y., Craft, A.M., and Cahan, P. (2018). A single cell transcriptional portrait of embryoid body differentiation and comparison to progenitors of the developing embryo. Stem Cell Res. *31*, 201–215.
Street, K., Risso, D., Fletcher, R.B., Das, D., Ngai, J., Yosef, N., Purdom, E., and Dudoit, S. (2018). Slingshot: cell lineage and pseudotime inference for single-cell transcriptomics. BMC Genomics *19*, 477.
Takahashi, Y., Hiraoka, S., Kitajima, S., Inoue, T., Kanno, J., and Saga, Y. (2005). Differential contributions of Mesp1 and Mesp2 to the epithelialization and rostro-caudal patterning of somites. Development *132*, 787–796.
Takahashi, Y., Yasuhiko, Y., Kitajima, S., Kanno, J., and Saga, Y. (2007). Appropriate suppression of Notch signaling by Mesp factors is essential for stripe pattern formation leading to segment boundary formation. Dev. Biol. *304*, 593–603.
Tan, Y., and Cahan, P. (2019). SingleCellNet: A Computational Tool to Classify Single Cell RNA-Seq Data Across Platforms and Across Species. Cell Syst. *9*, 207–213.e2.
Tropepe, V., Hitoshi, S., Sirard, C., Mak, T.W., Rossant, J., and van der Kooy, D. (2001). Direct neural fate specification from embryonic stem cells: a primitive mammalian neural stem cell stage acquired through a default mechanism. Neuron *30*, 65–78.
Wang, Y., Lin, L., Lai, H., Parada, L.F., and Lei, L. (2013). Transcription factor Sox11 is essential for both embryonic and adult neurogenesis. Dev. Dyn. *242*, 638–653.
Weirauch, M.T., Yang, A., Albu, M., Cote, A.G., Montenegro-Montero, A., Drewe, P., Najafabadi, H.S., Lambert, S.A., Mann, I., Cook, K., et al. (2014). Determination and inference of eukaryotic transcription factor sequence specificity. Cell *158*, 1431–1443.
Wilson, V., Manson, L., Skarnes, W.C., and Beddington, R.S. (1995). The T gene is necessary for normal mesodermal morphogenetic cell movements during gastrulation. Development *121*, 877–886.
Wolf, F.A., Angerer, P., and Theis, F.J. (2018). SCANPY: large-scale single-cell gene expression data analysis. Genome Biol. *19*, 15.
Yeo, J.-C., Jiang, J., Tan, Z.-Y., Yim, G.-R., Ng, J.-H., Göke, J., Kraus, P., Liang, H., Gonzales, K.A.U., Chong, H.-C., et al. (2014). Klf2 is an essential factor that sustains ground state pluripotency. Cell Stem Cell *14*, 864–872.
Zhang, K., Li, L., Huang, C., Shen, C., Tan, F., Xia, C., Liu, P., Rossant, J., and Jing, N. (2010). Distinct functions of BMP4 during different stages of mouse ES cell neural commitment. Development *137*, 2095–2105.
Zhu, Q., Song, L., Peng, G., Sun, N., Chen, J., Zhang, T., Sheng, N., Tang, W., Qian, C., Qiao, Y., et al. (2014). The transcription factor Pou3f1 promotes neural fate commitment via activation of neural lineage genes and inhibition of external signaling pathways. Elife *3*.